Optical versus infrared studies of dusty galaxies and active galactic nuclei - I. Nebular emission lines

Vivienne Wild, Brent Groves, Timothy Heckman, Paule Sonnentrucker, Lee Armus, David Schiminovich, Benjamin Johnson, Lucimara Martins, Stephanie Lamassa

HAL Id: insu-03646080
https://insu.hal.science/insu-03646080

Submitted on 20 Apr 2022

Optical versus infrared studies of dusty galaxies and active galactic nuclei – I. Nebular emission lines

Vivienne Wild,[1]* Brent Groves,[2] Timothy Heckman,[3] Paule Sonnentrucker,[3]
Lee Armus,[4] David Schiminovich,[5] Benjamin Johnson,[6] Lucimara Martins[7]
and Stephanie LaMassa[3]

[1]*Institut d'Astrophysique de Paris, CNRS, Université Pierre & Marie Curie, UMR 7095, 98bis bd Arago, 75014 Paris, France*
[2]*Leiden Observatory, Leiden University, PO Box 9513, 2300 RA Leiden, the Netherlands*
[3]*Department of Physics and Astronomy, Johns Hopkins University, Baltimore, MD 21218, USA*
[4]*Caltech, Spitzer Science Center, MS 314-6, Pasadena, CA 91125, USA*
[5]*Department of Astronomy, Columbia University, New York, NY 10027, USA*
[6]*Institute of Astronomy, Madingley Road, Cambridge CB3 0HA*
[7]*NAT-Universidade Cruzeirodo Sul, Sao Paulo, Brazil*

ABSTRACT

Optical nebular emission lines are commonly used to estimate the star formation rate of galaxies and the black hole accretion rate of their central active nuclei. The accuracy of the conversion from line strengths to physical properties depends upon the accuracy to which the lines can be corrected for dust attenuation. For studies of single galaxies with normal amounts of dust, most dust corrections result in the same derived properties within the errors. However, for statistical studies of populations of galaxies, or for studies of galaxies with higher dust contents, such as might be found in some classes of 'transition' galaxies, significant uncertainty arises from the dust attenuation correction. In this paper, we compare the strength of the predominantly unobscured mid-infrared [Ne II] $\lambda 15.5\,\mu m$+[Ne III] $\lambda 12.8\,\mu m$ emission lines to the optical Hα emission lines in four samples of galaxies: (i) ordinary star-forming galaxies (80 galaxies); (ii) optically selected dusty galaxies (11); (iii) ultraluminous infrared galaxies (6); and (iv) Seyfert 2 galaxies (20). We show that a single dust attenuation curve applied to all samples can correct the Hα luminosity for dust attenuation to a factor better than 2. Similarly, we compare [O IV] and [O III] luminosities to find that [O III] can be corrected to a factor better than 3. This shows that the total dust attenuation suffered by the active galactic nucleus narrow-line region is not significantly different from that suffered by the star-forming H II regions in the galaxy. We provide explicit dust attenuation corrections, together with errors, for [O II], [O III] and Hα. The best-fitting average attenuation curve is slightly greyer than the Milky Way extinction law, indicating either that external galaxies have slightly different typical dust properties from those of the Milky Way or that there is a significant contribution from scattering. Finally, we uncover an intriguing correlation between silicate absorption and Balmer decrement, two measures of dust in galaxies, which probe entirely different regimes in optical depth.

Key words: dust, extinction – galaxies: ISM – galaxies: star formation.

1 INTRODUCTION

In the last few decades, large optical spectroscopic surveys have dramatically improved our knowledge of the global distribution of galaxy physical properties, such as stellar mass, star formation rates (SFRs), star formation histories, and both gas phase and stellar metallicities. Furthermore, at low to intermediate redshifts, the sheer statistics of current optical spectroscopic surveys allow us to identify and study significant numbers of rare objects, which represent transient phases in the lifetime of galaxies: starburst, post-starburst and 'green-valley' galaxies, major mergers, and powerful active galactic nuclei (AGN). These transient phases, although rare, are globally important. For example, black hole growth occurs

*E-mail: wild@iap.fr

primarily in rare, high accretion rate events (Yu & Tremaine 2002; Heckman et al. 2004), and it is still debated whether the infrequent gas-rich galaxy major mergers are responsible for the morphological transformation of galaxies and the build-up of the red sequence (Wild et al. 2009; Eliche-Moral et al. 2010; Ilbert et al. 2010). In the near future, the James Webb Space Telescope (JWST) will allow rest-frame optical spectroscopic observations at high redshift, where galaxies are more active in both star formation and black hole growth.

There is an obvious benefit in using the information provided in the redshift survey to study the properties of the galaxies in detail. For example, when star formation is the dominant mechanism of excitation, Hα is a very simple and reliable measure of the SFR in galaxies. However, it must be accurately corrected for dust attenuation. In ordinary galaxies, the tight relations between dust-corrected Hα and other indicators of the SFR from other wavelength regimes provide circumstantial evidence that dust attenuation in the optical can be corrected for accurately. Kennicutt et al. (2009) suggests that errors on SFRs caused by the assumed dust curve (attenuation as a function of wavelength) can be ±10–20 per cent for typical star-forming galaxies in the local Universe. However, knowing the 'correct' dust curve is crucial. Muzzin et al. (2009) found that the use of different dust curves in spectral energy distribution (SED) fitting of high-redshift K-selected galaxies can alter parameters, such as SFRs and star formation time-scales by factors of 2–3. The large errors reported in this study result from the fact that the 'correct' dust curve to use at high redshift is largely unconstrained and there is a large range in the steepness of dust curves observed along lines-of-sight to stars in the Magellanic clouds and Milky Way.

With the complex physical processes that occur during transient phases in the lifecycle of a galaxy, it is uncertain how far rest-frame optical studies alone can help us in understanding their true impact. As dust content increases, and galaxy geometries become more complicated, corrections for dust attenuation become more uncertain. How much physical information can we really infer from optical data alone when faced with extreme star formation, dust production, AGN activity and complicated spatial geometries of disturbed galaxies?

In this paper, we compare emission-line fluxes in the optical to those in the mid-infrared (mid-IR), where dust attenuation is negligible, except in small and well-known wavelength bands. To test the recovery of Hα luminosity from optical data in the presence of significant dust, we compare and contrast a low-z 'representative' sample of galaxies with (i) dusty galaxies selected from the Sloan Digital Sky Survey (SDSS) based on their Balmer emission-line ratios and strong Balmer absorption lines, indicating a possible recent decrease in star formation; (ii) local ultraluminous infrared galaxies (ULIRGs) selected from the *Infrared Astronomy Satellite* (*IRAS*) bright galaxy sample (BGS) based on their total IR luminosities ($L_{TIR} > 10^{12}$). The control sample of galaxies arise from the Spitzer-SDSS-GALEX Spectroscopic Survey (SSGSS) and were chosen to be 'representative' of the ordinary galaxies within the SDSS and GALEX surveys. For the AGN in these samples, we further compare the [O III]/[O IV] line ratio to a sample of Seyfert 2 galaxies, to test the recovery of black hole accretion rates (BHARs) from the optical [O III] emission line. In a companion paper, we will address the effect of dust on the optical continuum, and thus estimations of star formation histories, and compare the SFRs derived from the multiwavelength continuum with those from Hα luminosity.

Understanding our selected 'unusual' galaxies is crucial for understanding galaxy evolution. The Balmer-strong galaxies show op-

tical emission lines indicating obscured AGNs, and the correction of their [O III] emission for dust attenuation using different dust curves results in contributing between an insignificant ∼1 per cent and a much more significant ∼10 per cent to the total [O III] luminosity (or BHAR) of all narrow-line AGNs in the SDSS. This has important implications for the starburst–AGN connection, for example, as the strong Balmer absorption lines suggest, this accretion is happening after the starburst has decayed (Wild et al. 2010). Low-z ULIRGs are usually associated with major gas-rich mergers (Sanders et al. 1988). Some models of galaxy evolution have used gas-rich major mergers as the driving force to change the observational properties of the galaxy population over cosmic time. The mergers lead to powerful starbursts and quasi-stellar object driven outflows, resulting in the population of red, quiescent ellipticals seen in the local universe (e.g. Hopkins et al. 2006; Naab, Khochfar & Burkert 2006). ULIRGs become increasingly common at earlier epochs and dominate the SFR density beyond $z \sim 1$ (Borgne et al. 2009). Understanding the basic properties of ULIRGs at low redshift and the limitations of the optical wavelength regime for identifying and understanding the properties of their power sources is crucial in an era when near-infrared (NIR) ground-based spectrographs and the JWST will soon allow us to study galaxies with rest-frame optical spectra at increasingly early epochs.

The outline of this paper is as follows. After briefly reviewing the topic of dust extinction and attenuation in Section 2, we present the spectral analysis methods and four samples in detail in Section 3. In Section 4, we compare the data with a variety of different dust curves commonly used in the literature. We conclude in Section 5 by discussing the implications of our work for measuring SFRs, BHARs and identifying AGNs in optical spectroscopic surveys. Finally, we provide relations for correcting the [O II], [O III] and Hα emission lines using a measured Hα/Hβ flux ratio (Balmer decrement), assuming a single dust curve, which provides a good fit to all of the samples studied in this paper.

Throughout this paper, we quote line luminosities in erg s⁻¹ and masses in solar masses. Optical parameters for all samples have been extracted from the SDSS-DR7 and may differ from those in earlier releases due to updates in the SDSS reduction pipeline. All optical wavelengths are quoted as measured in a vacuum, in keeping with SDSS convention, optical wavelengths are given in low-resolution and mid-IR wavelengths in μm.

2 REVIEW OF DUST ATTENUATION LAWS

Dust grains in galaxies, which intercept and scatter stellar and nuclear light, complicate the analysis of integrated galaxy spectra. Optical light reaching the observer is effected by dust in three different ways: (i) absorption; (ii) scattering out of the line of sight; and (iii) scattering into the line of sight. The first two combined is usually termed as 'extinction' and all three combined is termed as 'attenuation'. The final 'effective attenuation' observed in the integrated light of galaxies results from the integration of attenuated light over all lines-of-sight to light sources throughout the entire galaxy.[1] In this section, we introduce the basics of the effects of dust on studying the integrated light from galaxies. Calzetti (2001)

---

[1] Throughout this paper, we use the term 'effective attenuation' to encompass all effects relating to the dust, that is, absorption and scattering, and geometrical effects. We note that this differs from some other papers, which apply the term to 'single-line-of-sight' attenuation.

gives an extensive recent review of the literature, although note that the terminology differs in places from that adopted here.

The effective attenuation A_λ, in magnitudes, at a given wavelength λ is given by

$$A_\lambda = -2.5 \log \left(\frac{I_{\lambda,\text{obs}}}{I_{\lambda,\text{intr}}} \right) \tag{1}$$

$$= -2.5 \log[\exp(-\tau_\lambda)], \tag{2}$$

where $I_{\lambda,\text{obs}}$ is the observed luminosity, $I_{\lambda,\text{intr}}$ is the intrinsic luminosity of the source and τ_λ is the effective optical depth of the dust.

Observationally, we measure the dimming and reddening of light from sources, thus deriving an effective attenuation or extinction curve k_λ:

$$k_\lambda = \frac{A_\lambda}{E(B-V)} \tag{3}$$

$$= \frac{E(\lambda - V)}{E(B-V)} + R_V, \tag{4}$$

where the colour excess is defined by $E(\lambda - V) \equiv A_\lambda - A_V$ and R_V is the total-to-selective extinction in the V band. In the case of extinction, R_V is a function of the grain composition, size and shape. In the case of effective attenuation observed in galaxies, it is additionally a function of the local geometry of the dust and light sources and global geometry of the galaxy (bulge and disc, and inclination). In this work, we will use the term 'dust curve' to mean either 'effective attenuation' or 'extinction' curve, depending on the particular curve under discussion.

The effective attenuation suffered by the ultraviolet (UV) to optical stellar continua of starburst galaxies, where the unattenuated stellar continuum is relatively well understood, has been measured empirically from the ratio of heavily attenuated to less attenuated spectra (Calzetti et al. 1994, 2000). The dust curve is found to be 'greyer' (i.e. flatter) than extinction curves measured along single lines-of-sight towards stars in the Milky Way (MW),[2] as expected from geometrical effects. Similarly, Charlot & Fall (2000, hereinafter CF00) fitted the ratio of far-infrared (FIR) to UV luminosities and UV slope in starburst galaxies to find an effective attenuation curve that is well fitted by the shallow power law $\tau_\lambda \propto \lambda^{-0.7}$.

However, dust curves derived from stellar continua are not necessarily suitable for the correction of nebular emission lines. In starburst galaxies, nebular emission lines are found to be more attenuated than the stellar continua (e.g. Calzetti et al. 1994), indicating that the light passes through a greater quantity, and possibly different distribution or composition, of dust. Any difference in the distribution or composition of dust will result in a different shape for the dust attenuation curve and therefore errors in the correction of nebular emission lines using a dust curve derived from the stellar continua. The stronger attenuation of nebular emission lines, compared to the stellar continuum, can be successfully reproduced by models in which dust is distributed primarily in two components: diffuse interstellar dust and stellar birth clouds, which disperse after a finite time ($\sim 10^7$ yr) (Calzetti et al. 1994; Silva et al. 1998; CF00). This allows the emission lines, which are ionized by the hottest stars still enveloped in their dense birth clouds, to experience greater attenuation than the UV stellar continua, which has

an additional contribution from cooler stars around which the birth clouds have already dispersed.

In Wild et al. (2007), we presented explicitly the form of the dust curve for the correction of nebular emission lines in the CF00 dust model:

$$\frac{\tau_\lambda}{\tau_V} = \frac{A_\lambda}{A_V} = (1 - \mu) \left(\frac{\lambda}{\lambda_V} \right)^{-n} + \mu \left(\frac{\lambda}{\lambda_V} \right)^{-m}. \tag{5}$$

We reiterate that we use τ_V to refer to the final 'effective attenuation' suffered by light, including geometrical effects, and that this model is strictly an 'angle averaged' model, averaging over all sight-lines through a galaxy. The first term describes the slope of the screen-like extinction suffered as the light leaves the stellar birth-clouds and the exponent is set to match the extinction observed along lines of sight in the MW ($n = 1.3$). The second term describes the additional, much greyer attenuation caused by the intervening diffuse interstellar medium (ISM), where CF00 derived a best-fitting exponent of $m = 0.7$. The fraction of the total effective optical depth at 5500 low-resolution caused by dust in the diffuse ISM is controlled by the parameter μ. CF00 showed that the typical value for μ in their starburst data set was about 0.3. The resulting model attenuation curve, labelled $\mu_{0.3}$ throughout this paper, naturally lies between the pure continuum $\tau_\lambda \propto \lambda^{-0.7}$ attenuation (equivalent to $\mu = 1$) and pure screen-like attenuation (equivalent to $\mu = 0$).

Recently, da Cunha, Charlot & Elbaz (2008) applied and extended the two-component CF00 dust model to a sample of local galaxies with multiwavelength photometry and optical Hα and Hβ emission-line measurements, finding an excellent match to the data.

We note that an additional complication arises in the case of nebular emission from the narrow-line region (NLR) of an AGN, where a different dust geometry could lead to a different effective attenuation curve from that found for nebular emission from H II regions. Additionally, for galaxies with contributions to nebular emission from both star formation and an AGN NLR, the use of the Balmer decrement for the correction of NLR emission lines may be somewhat inappropriate. In general, it is reasonably assumed that the hydrogen recombination lines are dominated by the emission from H II regions in all but the strongest AGNs. However, this is not the case for higher ionization and higher excitation lines, where emission from the NLR can dominate. Thus, while the Balmer decrement will show how much dust is in H II regions, there is no reason to believe that light from the NLR would pass through the same amount of dust.[3] Therefore, the extinction correction applied to these other lines, such as [O III]λ5007 Å, may be incorrect. We investigate these effects in Section 4.4.

2.1 Attenuation of nebular emission lines

In order to determine the amount of attenuation suffered by optical nebular emission lines, ideally, one would observe a pair of lines whose intrinsic ratio is independent of physical conditions and where one of the pair lies at a wavelength long enough that attenuation is negligible (see also discussion in Osterbrock & Ferland 2006). Hydrogen recombination line ratios that include one line in the NIR wavelength range have been shown to be a powerful tool for constraining the dust attenuation curves for nebular emission lines in galaxies (Calzetti, Kinney & Storchi-Bergmann

---

[2] Commonly used MW extinction curves include Seaton (1979), Cardelli, Clayton & Mathis (1989) and O'Donnell (1994).

[3] The difference in the intrinsic Balmer decrements between NLR and H II regions (due to different gas temperatures) will be small relative to the difference caused by attenuation.

1996; Calzetti 2001). The data are well fitted by a screen-like MW extinction curve, which has since been favoured for the correction of emission lines for dust attenuation. These results suggest that a substantial fraction of the attenuation of emission lines must arise from dust in a foreground screen-like geometry (e.g. the birth clouds in the CF00 model). However, the samples studied to date have been small, containing only local starburst galaxies. Extending this study to a larger sample of galaxies, including more ordinary star-forming galaxies and dustier galaxies, is the purpose of this paper.

Sample sizes using ground-based NIR observations are restricted primarily by the difficulty resulting from contamination of observations by OH sky lines. *Hubble Space Telescope* observations of the NIR Paschen α line have been used to reveal the detailed distribution of star formation in galaxies relatively unimpeded by dust (Böker et al. 1999). The detection of dust lanes in some galaxies in this sample indicates that some level of extinction still exists even at 1.875 μm. Uncertainties in the form of dust curve in the NIR regime therefore cause a small additional source of uncertainty when using NIR emission lines to constrain dust curves in the optical.

With the launch of the *Spitzer Space Telescope*, with the Infrared Spectrograph (IRS, Houck et al. 2004) onboard, high-quality, moderate-resolution mid-IR spectra are available for the first time for a large number of low-z galaxies. Extinction in the mid-IR is negligible, except in small wavelength regions centred on 9.7 and 18 μm, where strong absorption can arise from the stretching and bending modes of amorphous silicate grains. While H recombination lines are found in the mid-IR, they unfortunately tend to be too weak to be easily measured. Two of the strongest and easily observable emission lines in the mid-IR arise from neon: [Ne II] 12.8 μm and [Ne III] 15.5 μm. In typical H II regions, over 95 per cent of neon is in these two states (Ne^+ and Ne^{2+}), thus we expect that the sum of these two lines will trace very well the ionized gas, and thus Hα, in galaxies. Indeed, Ho & Keto (2007) have already suggested that these mid-IR Neon lines could provide a useful new indicator of the SFR in galaxies. They have shown that [Ne II]+[Ne III] luminosity correlates strongly with both total IR luminosity in galaxies and the NIR Brα emission line in giant H II regions. Díaz-Santos et al. (2010) have shown that [Ne II] luminosity correlates strongly with that of Paα in star-forming regions in luminous infrared galaxies. Neon has the added benefit of being an abundant element, especially as it is not depleted on to dust grains. Therefore, in this work, we use the sum of these two lines as a tracer of the *unextinguished* emission from ionized gas in these galaxies. Although these lines lie on the edge of the silicate absorption features, in general, the extinction caused by this is minimal as we verify in Section 3. Combining *Spitzer* spectra with optical SDSS spectra provides a new and extremely powerful data set, in which both optical and mid-IR emission lines have been measured much more accurately than was possible in the past.

Starburst/H II region modelling (Kewley et al. 2001; Levesque, Kewley & Larson 2010) suggests that for typical twice solar metallicity H II regions, the ratio $L([Ne II]+[Ne III])/L(H\alpha)$ should be between 0.5 and 1.0, demonstrating how luminous the mid-IR Ne lines are. The range is caused by ionization effects, arising from different stellar models, the mean age of the ionizing stellar population and ionizing flux densities. There is one major disadvantage of using the [Ne]-to-Hα ratio to constrain the optical dust curve in galaxies in that the intrinsic ratio is directly dependent upon the metallicity of the gas, greatly expanding the range of possible values. For solar metallicity H II regions, the models predict that $L([Ne II]+[Ne III])/L(H\alpha)$ should be smaller by a factor of 0.6. However, we expect that this is not a dominant concern in the sam-

ples studied in this paper as we are exploring massive, dusty, and therefore metal-rich, galaxies. We discuss the impact of variations in the intrinsic ratio where relevant. We refer the reader to Ho & Keto (2007) for further details on the formation of the neon lines in H II regions.

In AGNs, the ionizing spectrum is much harder than found in star-forming regions, meaning that neon starts to populate higher ionization states. The sum of the mid-IR neon lines still traces the ionized gas very well, but the ionization is offset to higher values due to the harder radiation field. In addition, the harder radiation field of AGNs also creates partially (or X-ray) ionized regions, which have a higher $L([[Ne II]])/L(H\alpha)$ ratio. AGN photoionization models suggest $L([Ne II]+[Ne III])/L(H\alpha) \sim 2$, a factor of 2–4 higher than H II regions (Groves, Dopita & Sutherland 2004).[4] Again, we will indicate the effect of this result where relevant.

3 THE SAMPLES

In this section, we give the methodology used to measure the nebular emission lines, followed by the selection criteria of our four samples of galaxies. All samples have SDSS optical five-band imaging and fibre spectroscopy, together with *Spitzer* IRS spectroscopy. The SDSS specobjid, SDSS-MPA rowindex, RA and Dec. of the Balmer-strong, ULIRG and Seyfert samples are given in Tables A1–A3 to allow easy identification of the objects in the catalogues used in this paper. The equivalent information for the SSGSS sample is available online at http://www.astro.columbia.edu/ssgss. For a quick visualization of the samples: Fig. 1 presents their distributions in redshift, stellar mass and Balmer decrement (Hα/Hβ flux ratio), Fig. 2 shows their positions on the BPT diagram ([N II]/Hα versus [O III]/Hβ emission-line flux ratios, Baldwin, Phillips & Terlevich 1981) and in Fig. 3, we place all our samples on the Spoon et al. (2007) diagram of PAH$_{6.2}$ equivalent width (EW) versus the strength of the 9.7-μm silicate absorption. We discuss these figures further in Section 3.5.

The raw optical emission-line measurements for all SDSS-DR7 galaxies are provided on the SDSS-MPA web pages[5] and details are given in Kauffmann et al. (2003) and Brinchmann et al. (2004); errors have been rescaled according to the information provided on the web site. Note that all broad emission-line objects have been identified by the SDSS automated pipeline and are not included within the SDSS-MPA sample. Briefly, spectral synthesis models [Bruzual & Charlot (2003); 2008 version using the MILES spectral library, Sánchez-Blázquez et al. (2006)] are used to fit the stellar continuum, including stellar absorption features, and emission lines are measured from the residual of the data and model fit. Therefore *underlying stellar absorption is accurately accounted for when measuring optical emission-line fluxes*. Intervening Galactic extinction is corrected for prior to the calculation of the emission-line fluxes. The quality of the fits obtained is excellent.

For all samples, IRS spectroscopy was carried out in staring mode and 1D spectra were extracted using the standard Spitzer IRS Custom Extraction (SPICE). For the Balmer-strong galaxies the 'optimal extraction' option was chosen (Narron, Ogle & Laher 2007), which weights the extraction by the object profile and the signal-to-noise ratio (S/N) of each pixel and is suitable for faint sources. Individual 1D spectra were combined using custom algorithms.

---

[4] These line-ratio predictions can be obtained using the publicly available ITERA software package (Groves & Allen 2010).
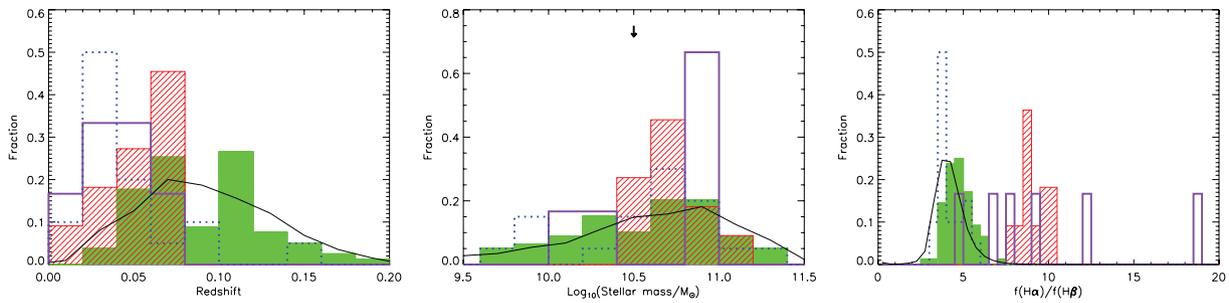
[5] http://www.mpa-garching.mpg.de/SDSS/DR7

Figure 1. The distribution of redshifts (left-hand panel), stellar masses measured from SDSS five-band optical photometry (middle panel) and Hα/Hβ ratios (right-hand panel) of the four galaxy samples: SSGSS (green, shaded), Balmer-strong (red, line-filled), ULIRG (purple) and Seyfert (blue, dotted). The black line shows the distributions for SDSS-DR7 galaxies, which have been spectroscopically observed and have a spectral $S/N_g > 8$. The downward arrow in the middle panel shows the position of the observed bimodality in the galaxy mass distribution (because the histograms are not corrected for sample incompleteness, the bimodality is not noticeable in this figure).
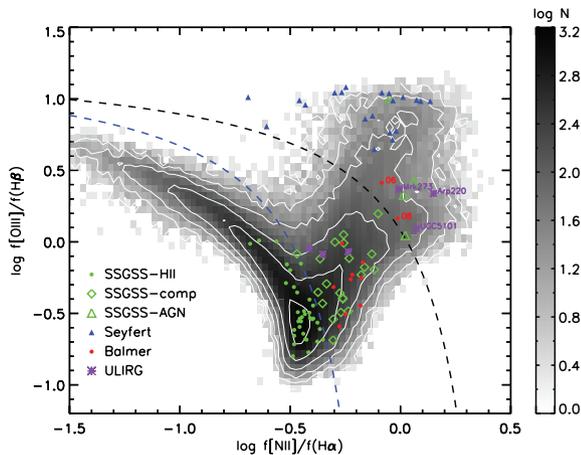

Figure 2. The BPT diagram (Baldwin et al. 1981): the narrow emission-line flux ratios $BPT_x = f[N\,II]_{\lambda6585}/f(H\alpha)_{\lambda6565}$ and $BPT_y = f[O\,III]_{\lambda5008}/f(H\beta)_{\lambda4863}$ for the SDSS-DR7 spectroscopic galaxy sample (grey-scale), SSGSS star-forming galaxies (green dots, 35/35), SSGSS AGN (green open triangles, 4/4), SSGSS composite galaxies (green open diamonds, 21/21), Balmer-strong galaxies (red dots, 11/11), ULIRGs (purple stars, 6/6) and Seyferts (blue triangles, 20/20). Only galaxies with all four lines detected at $>3\sigma$ confidence are plotted. The dashed lines indicate our division between star-forming/composite (blue) and composite/AGN (black) samples. These demarcation lines define the three optical classes (star-forming, composite, AGNs). To aid the discussion, the Balmer-strong galaxies and ULIRGs in the AGN region have been labelled.

To maximize consistency between the heterogeneous samples in this paper, the final low-resolution 1D spectra of all samples were reanalysed using the same custom algorithms and analysis packages where appropriate. To obtain [Ne II] $\lambda15.5\,\mu m$ and [Ne III] $\lambda12.8\,\mu m$ fluxes for the SSGSS and Seyfert samples, we used the mid-IR spectral fitting package PAHFIT (v1.2, Smith et al. 2007), which fits Gaussian profiles with widths set according to the instrument module. PAHFIT was run in the rest frame using a screen-like dust model and although dust attenuation is tiny at the wavelengths of the Ne lines, for complete consistency between samples, we removed the correction applied by the code (equation 4, Smith et al. 2007). Our final results are unchanged whether the minimal dust correction is applied or not. Where high-resolution spectroscopy is available, we use the high-resolution measurements of [Ne II] and [Ne III] due to the smaller error bars. For the Balmer-strong sample, the [Ne II] and [Ne III] emission-line fluxes were measured interactively from the short-high (SH) IRS spectra using the two-step baseline and
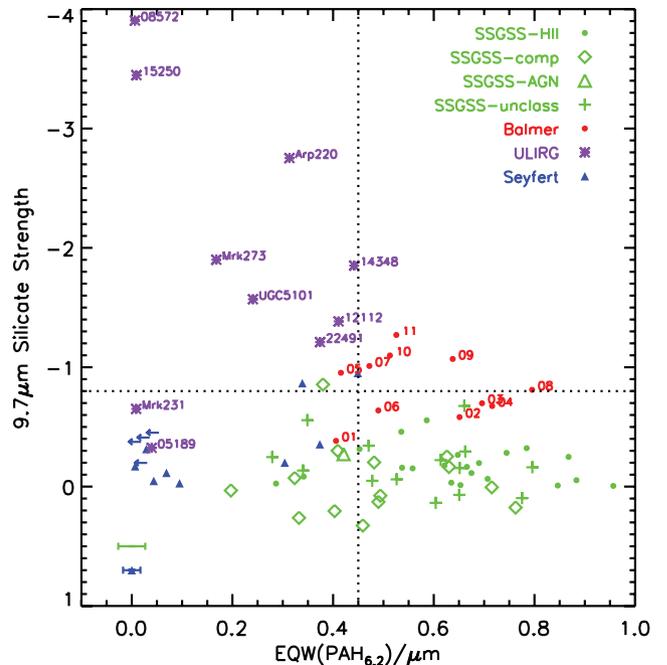

Figure 3. The strength of the 9.7-μm silicate absorption versus the EW of the 6.2-μm PAH feature, following the measurement methods presented in Spoon et al. (2007). Note that the *x*-axis is linear in order to better distinguish our samples. The dotted lines are two of the dividing lines given by Spoon et al. (2007) to separate galaxies with no-significant silicate absorption (horizontal) and ordinary star-forming/starburst galaxies (vertical). Median errors are shown in the bottom left-hand panel for the Seyfert and SSGSS samples, median errors are smaller than the symbol size for the Balmer-strong and ULIRG samples. Only those galaxies with mean per-pixel-S/N > 2 between 5.4 and 5.9 μm are plotted. Symbols are: SSGSS star-forming galaxies (green dots, 25/35), SSGSS AGN (green open triangles, 2/4), SSGSS composite galaxies (green open diamonds, 14/21), SSGSS galaxies with insufficient S/N in one or more optical emission lines to provide an optical BPT classification (green crosses, 20/20), Balmer-strong galaxies (red dots, 11/11, labelled), ULIRGs (purple stars, 6/6, labelled) and Seyferts (blue triangles, and upper limits marked by blue arrows, 13/20).

Gaussian line-fitting module from the SMART IDEA package (Higdon et al. 2004).[6] For the ULIRG sample, fluxes were taken from high-resolution spectroscopy, given in table 4 of Armus et al. (2007).

[6] http://isc.astro.cornell.edu/SmartDoc/LineFitting

To ensure consistency between the four samples, where possible,[7] we verified that [Ne II] and [Ne III] fluxes measured with PAHFIT or directly from the low-resolution spectra for the Balmer-strong and ULIRG samples were equal within the errors to those measured from the high-resolution spectra (with and without the minimal correction for attenuation applied in PAHFIT). For the Seyfert sample, [Ne II] λ15.5 μm fluxes were found to match within the errors those measured in the high-resolution mode, given in table 6 of LaMassa et al. (2010).

[O IV] λ26 μm was measured from high-resolution (LH) IRS spectroscopy in all cases (measurement from the low-resolution spectra is not possible due to a nearby Fe II line). For the Balmer-strong sample, [O IV] line fluxes were measured interactively using the SMART IDEA package as described above. For the ULIRG and Seyfert samples [O IV] line fluxes were taken from the tables in Armus et al. (2007) and LaMassa et al. (2010), respectively.

One of the major components of a star-forming galaxy spectrum in the mid-IR is the broad emission features generally accepted to result from the vibrational modes of polycyclic aromatic hydrocarbons (PAHs). While we do not study the PAH features in detail in this paper, PAHFIT outputs their fluxes and EWs, which we use to provide further clarification of the nature of our objects where necessary.

To visualize the different dust and AGN properties of our different samples in Section 3.5, we measure the EW of $PAH_{6.2}$ and the strength of the 9.7-μm silicate absorption. We attempted in both cases to follow closely the methods as described in Spoon et al. (2007), and we used the ULIRG sample to verify that our results are consistent with those given in Spoon et al. (2007) over the full range of the measurements.

3.1 The SSGSS sample

Our control sample is the Spitzer-SDSS-GALEX Spectroscopic Survey (SSGSS, O'Dowd et al. 2009; Johnson et al. 2009), a Spitzer Legacy survey (P.I. D. Schiminovich) which targeted 100 'ordinary' galaxies from the SDSS spectroscopic survey and GALEX surveys for follow-up mid-IR spectroscopy with the IRS (Houck et al. 2004) using the *Spitzer Space Telescope*. The galaxies are magnitude limited to the SDSS spectroscopic magnitude limit of $r < 17.7$ and additionally were selected to have GALEX-NUV fluxes >1.5 mJy for the faint sample (40 galaxies) and >5 mJy for the bright sample (60 galaxies). They were chosen, such that their mass, colour, SFR and redshift distribution are representatives of galaxies in the SDSS survey. A description of the survey, together with data tables containing SDSS and mid-IR measurements and derived parameters, are available at the team website.[8] In this paper, we make use of the IRS low-resolution spectroscopy of 80 SSGSS galaxies. The IRS spectra of the remaining galaxies are either incomplete due to problems during observations or reductions or suffer from considerable noise at short wavelengths, five of these caused by a solar flare. Further, four galaxies with median per-pixel-S/N < 10 in their SDSS spectra are removed, as the spectra were of insufficient S/N to allow accurate stellar continuum fitting around the Balmer emission lines. Further details of the SSGSS can be found in O'Dowd et al. (2009) and Johnson et al. (2009).

3.2 The dusty Balmer-strong sample

Our first sample of galaxies with significant dust contents are 12 Balmer-strong galaxies selected from the SDSS-DR4 to have an observed Hα/Hβ flux ratios greater than 8 (where a ratio close to 3 indicates little dust) and optical line ratios that indicated the possible presence of an AGN. Additionally, they were selected to have strong Balmer absorption lines, which might indicate a recent sharp decline in the SFR ('post-starburst'). However, the strong Balmer absorption lines might alternatively be caused by unusual dust properties rather than the star formation history (e.g. as postulated in Poggianti & Wu 2000). This is the subject of a future paper. Both high- and low-resolution IRS spectra were obtained for all of these 12 galaxies during *Spitzer* Cycle-4 (P.I. T. Heckman). Further observational details of this sample are provided in Appendix B. One of the 12 galaxies was subsequently discovered to have double-peaked narrow Hα and [N II] lines, together with significant underlying broad emission, which was not accounted for in the original emission-line measurements. Its IRS spectrum is dominated by emission from the AGN. Attempts to robustly remeasure the Hβ line accounting for the double peak were unsuccessful due to significant stellar absorption and its Ne/Hα and PAH/Hα ratios suggest that it is not in fact unusually dusty. We therefore remove it from all further discussion, leaving 11 Balmer-strong galaxies.

3.3 The ULIRGS

Our second sample of dusty galaxies is composed of 10 ULIRGs ($L_{IR} > 10^{12} L_{\odot}$) from the IRAS Bright Galaxy Sample (Soifer et al. 1987); the Spitzer IRS low- and high-resolution observations of these galaxies have been presented in detail in Armus et al. (2007). Of the 10 BGS ULIRGs, six are found in the SDSS spectroscopic sample [IRAS 15327+2340 (Arp 220), IRAS 08572+3915, IRAS 15250+3609, IRAS 09320+6134 (UGC 5101) and IRAS 12112+0305], three do not lie within the SDSS footprint (IRAS 05189−2524, IRAS 22491−1808 and IRAS 14348−1445) and one is optically too faint to have been targeted [IRAS 12540+5708 (Mrk 231) has an SDSS *r*-band magnitude of 19.4]. All six of the ULIRGs with SDSS spectra are late-stage mergers (Veilleux, Kim & Sanders 2002).

3.4 The Seyfert sample

In Section 4.4, we compare the high-ionization emission lines in the dusty galaxies with those of a sample of relatively dust-free (low Balmer decrement) Seyfert galaxies. This is composed of the top 20 [O III]λ5007 flux emitters out of all SDSS-DR4 main-sample galaxies classified as Seyfert galaxies based on their position on the BPT diagram. They have [O III] fluxes greater than 4×10^{-14} erg s^{-1} cm^{-2}, corresponding to a luminosity of $\sim 10^{41}$ erg s^{-1} at the median redshift of the sample. Both high- and low-resolution IRS spectra were obtained with high S/N. Further details of the Seyfert sample, along with a study of their X-ray properties, can be found in LaMassa et al. (2009) and LaMassa et al. (2010).

3.5 Sample comparison

The samples that we will compare and contrast in this paper were targeted for different purposes and thus any conclusions drawn must take into account potential systematics caused by their different selections.

---

[7] We found that PAHFIT does not fit the continuum well for ULIRGs with strong silicate absorption and therefore the emission-line measurements were unreliable in these cases.

[8] http://www.astro.columbia.edu/ssgss/

The redshift distribution of the four samples is shown in the left-hand panel of Fig. 1. The black line shows the redshift distribution of the SDSS spectroscopic galaxy catalogue with *r*-band extinction-corrected petrosian magnitude[9] in the range $14.5 < r < 17.77$. The Seyfert and ULIRG sample are flux limited in nebular emission and IR flux, respectively, and lie predominantly at low redshifts. The SSGSS galaxies were selected to be representatives of the full SDSS sample and therefore their redshift distribution tracks closely that of the full SDSS survey. The Balmer-strong sample is limited to $z < 0.07$ to ensure that the stellar population sampled by the optical fibre through which the spectrum is taken lies within the central region of the galaxy close to the AGN.

The stellar mass distribution of the four samples is shown in the middle panel of Fig. 1. The stellar masses[10] have been estimated from stellar population model fits to the optical five-band SDSS photometry, using a Bayesian analysis similar to that described in Kauffmann et al. (2003) and Salim et al. (2005). Most samples cover the full range in stellar mass probed by the SDSS, although the Balmer-strong galaxies do not cover the low-mass end of the distribution. Note that the histograms are *not* corrected for incompleteness effects due to sample or survey flux limits and therefore are not suitable for drawing conclusions about the underlying distributions of galaxy mass. To aid the reader, the position of the galaxy mass bimodality is marked by a downward arrow. The right-hand panel of Fig. 1 shows the Balmer decrement distributions of the four samples, showing how the Balmer-strong and ULIRG samples are significantly dustier on average than the SSGSS and Seyfert samples.

In Fig. 2, we show the position of the four samples on the BPT diagram, with the underlying grey-scale showing the distribution of spectroscopically observed galaxies in the SDSS. Only those galaxies with S/N > 3 in all four emission lines are plotted. This is the most commonly used optical diagram for diagnosing the presence of an AGN. Throughout this paper, we distinguish four classes of galaxies: (i) *AGN dominated*, with emission-line ratios, which place them above the stringent theoretical starburst criterion of Kewley et al. (2001) or have [N $\textsc{ii}$]/Hα > 0.0; (ii) *star-formation dominated*, which lie below the observationally determined demarcation line of Kauffmann et al. (2003), or have [N $\textsc{ii}$]/Hα < −0.5; (iii) *composite* objects, which lie between the AGN-dominated and star-forming-dominated samples; we term them 'composite' to indicate that the emission may be caused by a combination of both AGNs and star formation (Kauffmann et al. 2003, although see caution below); and (iv) *unclassified* objects with non-existent or weak (S/N < 3σ) emission lines, which do not allow classification into the first three samples.

We note that the BPT diagram does not provide a firm demarcation between the samples and that the demarcation lines are not motivated by robust theoretical predictions; we use the lines only to provide a convenient broad classification. Levesque et al. (2010) present up-to-date modelling of the 'maximum starburst' demarcation line, placing it much closer to the observed star-forming branch in the SDSS than the Kewley et al. (2001) line. Shocks, high metallicity and ionization by old stars can also cause galaxies to lie in the 'composite' class (Stasińska et al. 2008). We note that most of the

Balmer-strong galaxies have detectable molecular H$_2$ lines, as do the majority of ULIRGs (Higdon et al. 2006). In the case of ULIRGs, these lines are thought to arise primarily from photodissociation regions associated with star formation. The H$_2$/PAH flux ratio of the Balmer-strong galaxies is exactly that expected for star-forming galaxies (Ogle et al. 2010), indicating that shocks are similarly not a dominant excitation mechanism in the Balmer-strong galaxies. This suggests that the high [N $\textsc{ii}$]/Hα line ratios in these samples are in general caused by a central AGN, rather than shocks. S/N limits placed on emission lines may preferentially cause very high metallicity galaxies and LINERs caused by shocks and/or ionization by old stars to be 'unclassified' in the SSGSS sample (Fernandes et al. 2010). However, none of these caveats affect the results of this paper, which do not rely on a precise identification of weak AGNs or on the precise positioning of pure AGNs or star-forming galaxies on the BPT diagram. Where possible, we include unclassified SSGSS galaxies in the figures.

Out of the 80 SSGSS galaxies, four are AGN dominated, 21 are composite objects, 35 are star forming and 20 are unclassified. Out of the 11 Balmer-strong galaxies, two are AGN dominated and the remainder composite objects. Three ULIRGs are AGN dominated (Arp 220, Mrk 273 and UGC 5101) and three are composite objects (08572, 12112, 15250). All Seyferts clearly lie in the AGN-dominated region by definition. Fig. 2 supports our assumption that the intrinsic $L($[Ne $\textsc{ii}$]+[Ne $\textsc{iii}$]$)/L($Hα) ratio will not vary greatly between our samples. Most galaxies in the samples lie in the solar and greater region of this line ratio diagnostic diagram (Groves et al. 2006; Levesque et al. 2010).

Finally, in Fig. 3, we follow Spoon et al. (2007) and plot the EW of the 6.2-μm PAH feature against the strength of the 9.7-μm silicate absorption. We plot only those objects with mean S/N-per-pixel > 2 in the wavelength regions used to define the continuum for the measurement of the silicate absorption at 9.7 μm and with total flux/error >3 in the 6.2-μm PAH feature. The lower branch is interpreted as a mixing between AGNs and star formation activity and the upper branch as an evolution from a dust-obscured to dust-unobscured nuclear starburst or AGN (see Rowan-Robinson & Efstathiou 2009). Because of its focus on both dust and AGN activity, Fig. 3 is particularly useful for characterizing our four different samples.

Galaxies in the SSGSS occupy the bottom right-hand corner of the diagram as expected for 'ordinary' star-forming galaxies or weak narrow-line AGNs. They have strong EW(PAH$_{6.2}$) and weak silicate absorption. The composite galaxies in this sample have a lower mean EW(PAH$_{6.2}$) than the star-forming galaxies, strengthening the argument that these galaxies contain an AGN. The large scatter, and significant number of objects with apparent silicate emission, is indicative of the generally lower quality of these spectra compared to our other samples. SSGSS galaxies with optical emission lines, which are too weak to classify them on the optical BPT diagram, do not differ in mid-IR properties from their classified counterparts.

The Balmer-strong galaxies generally have stronger silicate absorption than SSGSS galaxies, placing them between the ULIRG and SSGSS samples and therefore within the common interpretation of the diagram, at the end of their evolution from a dusty starburst. M82 is the prototype galaxy for this region of the diagram.

The ULIRGs are a mixed group, as has been discussed at length in the literature. Although our sample is small, it is interesting to note that the ULIRGs with particularly strong silicate dust absorption (08572, 15250) show optical emission-line ratios indicative of a mixture of star formation and AGNs and/or shocks. Three out of the

---

[9] Petrosian magnitudes and radii are estimates of total magnitudes suitable for all types of galaxies. They are derived by the SDSS photometry pipelines, with details found at http://www.sdss.org/dr7/algorithms/photometry.html
[10] Courtesy of Jarle Brinchmann, publicly available at http://www.mpa-garching.mpg.de/SDSS/DR7/.

four ULIRGs with weaker silicate absorption (Arp 220, Mrk 273, UGC 5101) have AGN-dominated optical emission (i.e. implying little contribution from star formation, except possibly in the case of extreme shocks). This is consistent with the interpretation of the upper branch as an evolution from dusty starburst galaxies in the top left-hand side to galaxies undergoing less-intense, less-dusty star formation in the bottom right-hand side, with dust-obscured AGN activity occurring throughout the evolution.

The Seyferts are generally found to have very weak PAH EWs and little silicate absorption and therefore lie in the region of the diagram commonly interpreted as being occupied by strong AGNs, which heat the dust to high temperatures. 2/20 show some silicate absorption together with stronger EW(PAH$_{6.2}$). The median (mean) BPT$_y$ values of the four Seyferts with EW(PAH$_{6.2}$) > 0.2 are 0.78 (0.75), compared to 1.01 (0.99) for the remainder of the sample. This suggests that emission from star formation contributes to the optical emission lines even in the Seyfert branch of the BPT diagram. These results are consistent with the interpretation of the lower branch of Fig. 3 as mixing between AGNs and star formation activity.

3.6 Aperture corrections

'Aperture bias' describes the effects caused by the fact that a fixed aperture or slit width may probe only a small fraction of a galaxy's total light, and this fraction is a function of galaxy radius and redshift. The physical size probed by the SDSS 3-arcsec fibre varies from under 1 kpc for the majority of the ULIRG sample to around 10 kpc at the maximum redshift of the SSGSS galaxies. Fortunately, the results in this paper rely upon line ratios or EWs rather than absolute luminosities, and therefore aperture bias in this usual sense is less relevant.

However, comparing line strengths from the IRS spectra with those from the SDSS spectra leads to other aperture-related issues. The finite (and different) slit and fibre apertures may mean that the IRS and SDSS spectra sample a different fraction of the same galaxy, and this will cause measured line ratios to differ from the true values. There are two important issues: (i) light is lost from the slit/fibre due to the point spread function (PSF); and (ii) light is lost from the outer regions of extended sources, depending on the size of the aperture and the accurate positioning of the aperture on the source. In this paper, the precise flux calibration between the two data sets is relatively unimportant, but it is still important that we minimize any additional scatter in the observed relations. To help the reader to understand the limitations of our data, we outline here the flux-calibration procedures of the mid-IR and optical spectra.

The IRS PSF increases substantially from the blue to the red wavelength extremes of the instrument, and therefore each IRS slit has a different width designed so as not to lose too much of the light at the reddest ends.[11] The spectral extraction procedure accounts for the varying PSF along the slit by normalizing the flux at each wavelength according to the fraction of light missed from a calibration stellar point-source.

The SDSS DR7 spectra have been spectrophotometrically calibrated using the PSF magnitudes of stars observed on the same plate

as the galaxies (Adelman-McCarthy et al. 2008). To aid aperture corrections, the SDSS-MPA emission-line measurements have been recalibrated to the 3-arcsec fibre magnitudes. Therefore, to match the stellar PSF-normalized mid-IR spectra, we have removed this recalibration, returning the flux level of the SDSS emission lines to the stellar PSF-normalized values.

The use of stellar PSF spectrophotometric calibration for both optical and mid-IR spectra allows good relative calibration for point sources, but inaccuracies will still arise in the case of extended sources. For centrally concentrated sources, such as circumnuclear starbursts in ULIRGs or AGN NLR emission, the point-source approximation is a good one. However, for extended sources, the measured mid-IR to optical line ratios may depend on the relative size of the apertures and the relative surface brightness distribution of the sources. Both effects are difficult to correct for accurately, especially in the case of radial differences within the sources (e.g. in AGN versus star-forming nebular emission). We have therefore not attempted any further aperture correction and will caution the reader at points in the text where this effect may be relevant.

4 RESULTS

In Fig. 4, we plot Hα versus [Ne II] $\lambda15.5$ μm + [Ne III] $\lambda12.8$ μm (from now on [Ne]) luminosities for all of the samples, first with Hα uncorrected for dust attenuation and then corrected with five different dust curves selected from the literature to cover the full range in possible greyness. The panels are ordered by increasing greyness of the dust curve used, from the screen-like extinction curves [Small Magellanic Cloud (SMC) and MW] to galaxy continuum derived attenuation curves (Calzetti and $\lambda^{-0.7}$). The SMC curve was evaluated from the tabulated results of Pei (1992) with an $R_V = 3.1$; the MW curve was taken from O'Donnell (1994) with an $R_V = 3.1$; the $\mu_{0.3}$ curve is from Wild et al. (2007); the Calzetti curve is from Calzetti et al. (2000) with an $R_V = 4.05$; and the $\lambda^{-0.7}$ curve is from CF00 as discussed in Section 2.

In each panel, a maximum-likelihood best-fitting linear relation is fitted to the SSGSS-star-forming sample allowing for errors in both *x*- and *y*-axis quantities and fixing the intercept to be zero (dashed line). Twice and half the best-fitting [Ne] luminosity for each Hα luminosity is indicated as the dotted lines to aid comparison between the panels of the scatter between the two quantities. The best-fitting gradient (*g*, equal to the best-fitting intrinsic [Ne]/Hα ratio) and Pearson's correlation coefficient (*r*) are given in the bottom right-hand side of each panel, both evaluated using the SSGSS-star-forming sample only.

In panel (a), it is immediately evident that without correcting Hα for dust attenuation, the scatter between Hα and [Ne] emission luminosities is large, even for the SSGSS galaxies with normal levels of dust. For the dusty Balmer-strong and ULIRG samples, there is a clear excess of [Ne] for their observed Hα luminosity as expected for dusty galaxies.

As we move through the dust laws, from least- to most-grey [panels (b) to (f)], we see steady trends. The best-fitting intrinsic [Ne]/Hα ratio monotonically decreases and the correlation coefficient is maximal for the MW, $\mu_{0.3}$ and Calzetti dust curves. Focussing on the dusty Balmer-strong and ULIRG samples, we notice that these move from lying above the relation defined by the SSGSS-star-forming galaxies in panels (a) and (b) to lying below the relation in panel (f). This is caused by their under- and over-correction for dust attenuation using the different dust curves.

In Fig. 5, we show the samples more clearly by plotting the residual of the [Ne] luminosity from the linear fit using the MW, $\mu_{0.3}$
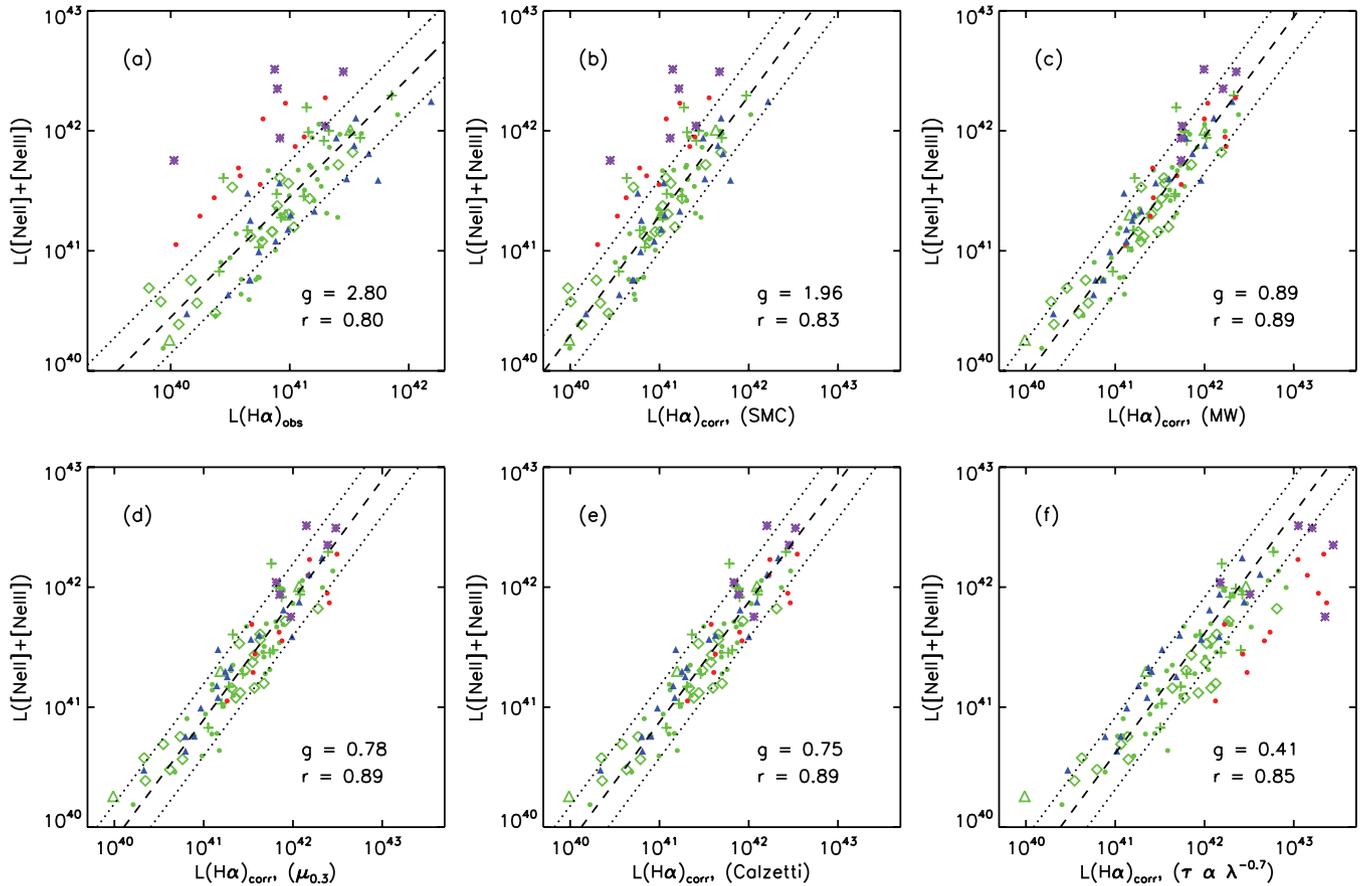
---

[11] The short-low IRS module covering the wavelength range 5.2–14.5 μm has a slit aperture of 3.6×57 arcsec^2. The long-low IRS module covering the wavelength range 14.0–38.0 μm has a slit aperture of 10.6×168 arcsec^2. At high resolution, the SH module covers 9.9–19.6 μm with a slit aperture of 4.7×11.3 arcsec^2 and the long-high (LH) module covers 18.7–37.2 μm with a slit aperture of 11.1×22.3 arcsec^2.

Figure 4. The optical Hα λ6565 versus mid-IR [Ne II] λ15.5 μm+[Ne III] λ12.8 μm luminosities in erg s^{-1}. Panel (a): with no correction of Hα for dust attenuation (note the different *x*-axis range in this panel). Panels (b–f): after correcting Hα for dust attenuation using different dust curves as described in the text; note the offset *x*-axis scales to panel (a). The panels are ordered by increasing 'greyness' of the dust curve used, from the screen-like SMC and MW extinction curves to the attenuation curves derived from the continua of starburst galaxies (Calzetti and $\tau \propto \lambda^{-0.7}$). See text for references to the particular dust curves. The dashed line shows a maximum-likelihood line fit to the *SSGSS-star-forming galaxies only*, with a factor of 2 above and below the best-fitting relation indicated by the dotted lines. The best-fitting slope to the *SSGSS-star-forming sample only* (*g*) is indicated in the bottom right-hand side of each panel, together with the Pearson correlation coefficient (*r*) for the *SSGSS-star-forming sample only*. The statistical errors on *g* are a few per cent. Only those galaxies with Ne, Hα and Hβ lines detected at >3σ are plotted. Symbols are: SSGSS star-forming galaxies (green dots, 35/35), SSGSS AGN (green open triangles, 3/4), SSGSS composite galaxies (green open diamonds, 19/21), Balmer-strong galaxies (red dots, 11/11), ULIRGs (purple stars, 6/6) and Seyferts (blue triangles, 19/20).

and Calzetti dust curves. The mean and variance of each sample in these figures is informative for comparing the different dust curves. For the dusty ULIRGs, the mean is 2.0, 1.6 and 1.5 for the MW, $\mu_{0.3}$ and Calzetti dust curves, respectively, that is, they are significantly offset for all dust curves (see below for further discussion). For the Balmer-strong sample, the mean is 1.1, 0.9 and 0.8, suggesting perhaps that a dust curve in between the MW and $\mu_{0.3}$ is most appropriate, but any offset between this extreme dusty sample and ordinary star-forming galaxies is very small. For the SSGSS star-forming sample, the mean is 1 by definition for all dust curves. The variance is ∼0.15 for all dust curves, that is, the scatter is less than a factor of 2 and there is no strong trend with Hα luminosity for the star formation dominated galaxies.

From these figures, we can identify the expected offset of the AGN caused by a higher intrinsic [Ne]/Hα ratio. For the Seyfert sample and $\mu_{0.3}$ dust curve, the mean offset is 1.26, that is, about a 25 per cent enhancement in [Ne] for their Hα luminosity. The magnitude of this offset does not correlate with the position on the BPT diagram or PAH EW, although the size of the sample is too small to rule out the possibility that those with a smaller

offset have a greater contribution to star formation in their lines. Averaged over the samples, the offset is seen only for the Seyfert galaxies, and the three SSGSS AGNs, which lie in or close to the Seyfert region on the BPT diagram. The SSGSS composite sample has a mean of 1 for all dust curves, which suggests that the AGN in general does not contribute significantly to the Ne/Hα line ratio in these composite galaxies. However, the trend upwards at low Hα luminosities is driven by composite objects, suggesting that there may be a small effect at low SFRs. The observed average enhancement in the [Ne]/Hα ratio of the ULIRGs noted above could be due to small number statistics, the dust curve (i.e. a shallower dust curve would be more appropriate) or the presence of deeply buried AGNs. We note that the ULIRGs are only offset by at most a factor of 3, that is, dust-corrected Hα luminosity tracks mid-IR [Ne] luminosity to better than a factor of 3 even in extreme dusty and disturbed objects. We will return to these points below.

The maximum-likelihood fits provide a measure of the dust-free ratio of [Ne] to Hα luminosity in our IRS/SDSS data sets, when star formation is the dominant excitation mechanism for the line
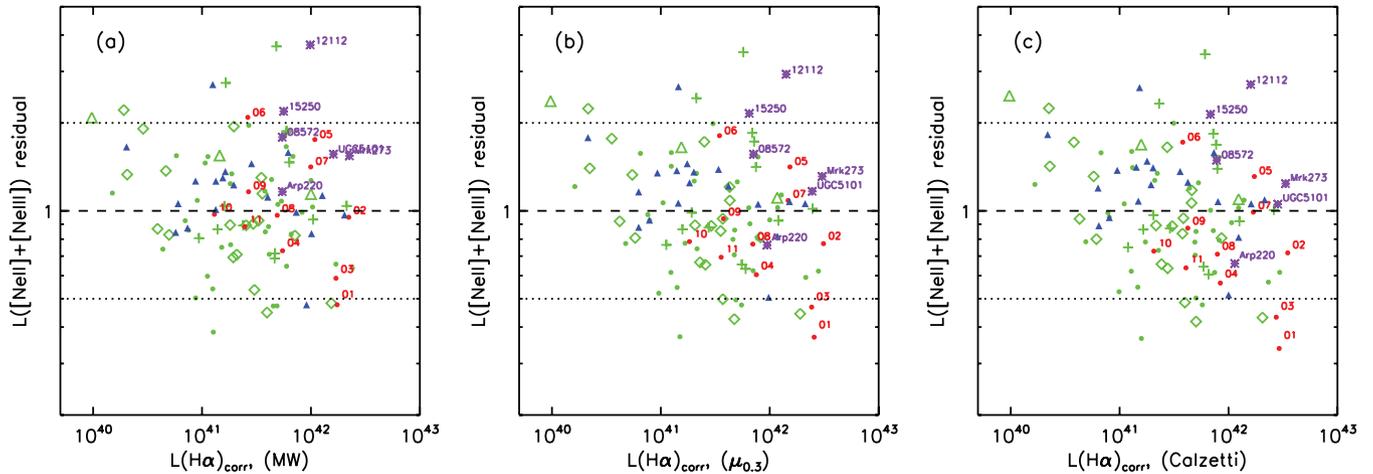
Figure 5. The residual [Ne] luminosity from the best-fitting linear relation between dust-corrected Hα and [Ne] luminosities, as a function of Hα luminosity in erg s^{-1}. From the left-hand to right-hand side, Hα has been corrected for dust attenuation using the MW, $\mu_{0.3}$ and Calzetti dust curves. The offset of the AGN-dominated sources from the star-formation-dominated sources is clear. The mean offset for the Seyfert sample is a factor of 1.26 for the $\mu_{0.3}$ dust curve. Symbols and lines are as in Fig. 4.

emission:

$$L[\text{Ne}] = g \times L(\text{H}\alpha)_{\text{corr}}, \qquad (6)$$

where $L[\text{Ne}] = L([\text{Ne\,II}]\,\lambda15.5\,\mu\text{m}) + L([\text{Ne\,III}]\,\lambda12.8\,\mu\text{m})$ and $g = 0.89, 0.78$ and 0.75 for the MW, $\mu_{0.3}$ and Calzetti dust curves, respectively. While it is encouraging that the measured intrinsic ratio lies exactly at the centre of the range predicted by the models for twice solar metallicity H II regions (see Section 2.1), a precise comparison between models and data would only be possible after much greater care has been taken to perform precise aperture corrections. In the case of the AGN, the emission-line source is point like and therefore the relative calibration between the mid-IR and optical spectra should be the most accurate. The fact that the average [Ne]/Hα ratio is a little lower than predicted may be due to contamination by star formation in a subset of the Seyfert sample (see Section 3.5).

In the following subsection, we study the differences between the dust curves in more detail.

4.1 Comparison of common dust attenuation laws

In Fig. 6, we plot the observed [Ne]/Hα versus Hα/Hβ luminosity ratios for all of our samples. In the left-hand panel, we use a logarithmic scale to allow the dustiest ULIRGs to appear. In the right-hand panel, we focus on the less-extreme objects and only include galaxies, where their optical emission-line ratios indicate that star formation is a significant emission-line source (classified as a composite or star forming in the optical BPT diagram, Fig. 2). Overplotted as the black lines are the predicted line ratios from the different dust curves presented in the previous subsection. In each case, the intrinsic [Ne]/Hα ratio is set from the fit to the SSGSS-star-forming galaxies as described above.

Although there are several factors, which can move galaxies within this diagram, dust has the strongest effect, increasing both the Balmer decrement and observed [Ne]/Hα ratio by an order of magnitude over the range probed by our samples. The different dust curves predict different relations between these two line ratios, even when we allow the intrinsic [Ne]/Hα ratio to be a free parameter fit by the data. As shown in the previous section, the MW, $\mu_{0.3}$ and

Calzetti dust curves provide the best fits to the SSGSS-star-forming galaxies. Fig. 6 shows that the $\mu_{0.3}$ and Calzetti attenuation curves also pass through the centre of the Balmer-strong sample.

The scatter of the SSGSS-star-forming galaxies about the best-fitting dust curves is large, and this may have several origins. First, the errors on the line flux measurements, particularly in Hβ, are significant. Secondly, we expect some variation due to different metallicities. The grey-shaded region shows the range predicted by the theoretical models for twice solar H II regions and the arrow in the left-hand panel shows how this region moves for solar H II regions. The three galaxies with the lowest measured [Ne]/Hα ratio lie significantly to the left-hand side of the 2-Z$_\odot$ prediction, but within the Z$_\odot$ prediction. These three galaxies also have some of the highest [O III]/Hβ and [Ne III]/[Ne II] ratios of the sample, indicative of harder ionization perhaps resulting from lower metallicity star formation. The single Seyfert galaxy with a [Ne]/Hα ratio less than 1 has the lowest [N II]/Hα ratio of the whole sample, unusually low for Seyfert galaxies, and likely associated with accretion of low-metallicity gas (Groves et al. 2006).

While low metallicities can explain the scatter of SSGSS-star-forming galaxies to the left of the dust-curve predictions, the scatter to the right is unlikely to be caused by metallicity variations as scatter in this direction requires significant and unlikely neon abundance increases (i.e. greater than twice solar). This leads us to the third, and most interesting, cause for scatter in the line ratio relation: intrinsic differences in the type or distribution of dust in galaxies.[12] In a two-component dust model, increasing the fraction of dust in the diffuse ISM relative to the dense birth clouds increases the contribution from scattering and makes the dust curve greyer. In the CF00 emission-line dust model given in equation 5, this relative amount of diffuse versus dense dust is controlled by the parameter μ. By increasing μ to 0.9 (i.e. 90 per cent of the effective optical depth from the dust comes from the ISM and 10 per cent from the stellar birth clouds), we can describe the lower envelope of the SSGSS galaxies. While this qualitative result is suggestive, a

---

[12] Face-on galaxy orientations can also cause increased scattering into the line of sight and thus greyer dust curves (Rocha et al. 2008).
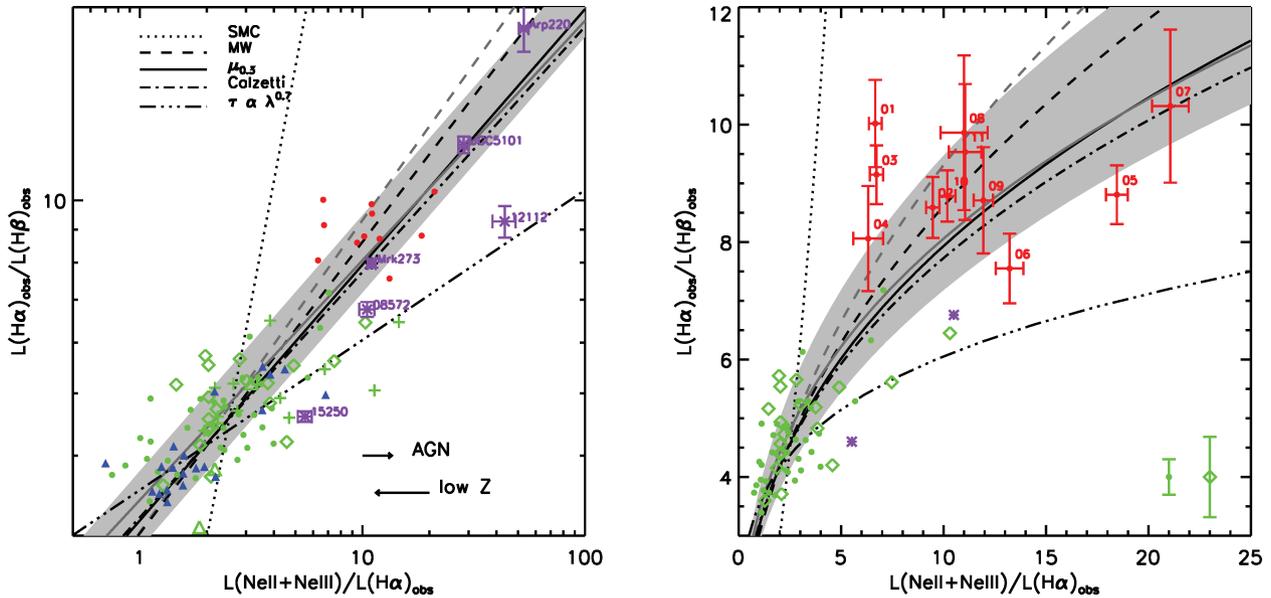
Figure 6. The observed [Ne]/Hα and Hα/Hβ flux ratios. Left-hand panel: A logarithmic scale allows all samples to appear, and all star-forming, AGNs, composite and unclassified objects are plotted. Right-hand panel: A linear version of the same plot, with the axes restricted to focus on the less-extreme galaxies. Only star-forming and composite galaxies are plotted. Overplotted as black lines are the predicted ratios from different dust curves: the SMC extinction curve with an $R_V = 3.1$ (Pei 1992); an MW extinction curve with $R_V = 3.1$ (O'Donnell 1994); the $\mu_{0.3}$ attenuation curve for emission lines (Wild et al. 2007); the Calzetti attenuation curve for starburst continua with $R_V = 4.05$ (Calzetti et al. 2000); and the $\lambda^{-0.7}$ attenuation curve for starburst continua from CF00. The grey lines additionally mark a different MW extinction curve with $R_V = 3.2$ (dashed grey, Seaton 1979; Nandy et al. 1975) and our new best-fitting dust curve from Section 4.2 (solid grey) with $\mu = 0.4$. In all cases, the intrinsic Ne/Hα ratio is taken from the best fit to the SSGSS-star-forming galaxies. The grey shaded region shows the theoretical range in observed [Ne]/Hα ratio for a twice solar stellar population and the $\mu_{0.3}$ dust curve, and the bottom arrow in the left-hand panel indicates the theoretical decrease in this ratio as metallicity decreases from twice solar to solar. The upper arrow in the left-hand panel indicates the average observed increase in the [Ne]/Hα ratio, where an AGN is the dominant ionization source (i.e. a factor of 1.26 observed for the Seyfert galaxies). For clarity, error bars are indicated for the ULIRGs in the left-hand panel, and for the Balmer-strong galaxies, in the right-hand panel. Median errors are indicated in the right-hand panel for the SSGSS star-forming and composite galaxies. Symbols are the same as in Fig. 4.

further detailed study including orientation, metallicity and ionization effects would be required to confirm that these galaxies do indeed have a significantly different dust geometry.

It is evident that the three ULIRGs classified as composite galaxies by their optical line ratios also appear to favour a greyer dust curve than the dusty Balmer-strong galaxies. However, as we discuss further below, it is also plausible that the high Ne/Hα ratio observed in these ULIRGs, as well as in some SSGSS-composite galaxies, is simply due to a deeply buried AGNs.

We summarize the results up to this point by noting that a single appropriate dust curve, combined with an accurately measured Balmer decrement, can recover the intrinsic optical emission-line luminosities to better than a factor of 2 in the majority of ordinary star-forming and dusty galaxies. Our data show that this remains true for galaxies with dust contents up to an A_V of 4.4. However, while the use of a MW, $\mu_{0.3}$ or Calzetti dust curves for large samples of galaxies will cause the least overall bias in the final dust-corrected emission-line luminosities, the effect of a greyer dust curve in individual galaxies should not be understated. A galaxy with a very typical measured Hα/Hβ ratio of 4.5 would have its Hα luminosity, and thus star-formation rate, corrected by a factor of around 2.5 using the average dust curve, whereas a factor of 7 would be more appropriate, if the majority of its dust were in the diffuse ISM.

4.2 Fitting the dust curve

Throughout the remainder of this paper, we will focus on results using the CF00 μ dust curve, as it allows greater flexibility than the

traditional dust curves in the calculation of errors, and the discussion of variations in dust curves within the sample as presented in the previous section. Additionally, it is the only dust curve specifically motivated and justified for the correction of nebular emission lines. The MW dust curve assumes a screen-like dust distribution, and the Calzetti dust curve is intended for correcting the continuum light from galaxies. Rather than assuming $\mu = 0.3$ as derived by CF00, we can fit the [Ne] versus Hα luminosities of the SSGSS-star-forming galaxies to obtain the best-fitting μ and intrinsic [Ne]/Hα ratio together with errors. We use a maximum-likelihood linear fit, accounting for errors on both quantities, and fix the intercept to be zero.[13] Formal, statistical errors on the derived μ are at the level of 5 per cent. The errors obtained from bootstrap resampling with replacement of the data are more significant and we quote these errors below, and use them to obtain errors on the dust correction formulae presented in Sections 5.1 and 5.2.

We find $\mu = 0.4 \pm 0.2$, that is, on average 40 per cent of the optical depth at 5500 Å arises in the ISM of the galaxies. This is consistent within the errors with $\mu = 0.3$ derived by CF00 for their sample of local starburst galaxies. The intrinsic [Ne]/Hα ratio fit at the same time is $g = 0.6 \pm 0.1$. The resulting curve is shown as the solid grey line in Fig. 6 and is explicitly given as

$$\frac{\tau_\lambda}{\tau_V} = \frac{A_\lambda}{A_V} = 0.6(\lambda/5500)^{-1.3} + 0.4(\lambda/5500)^{-0.7}, \qquad (7)$$

[13] Allowing the intercept to be non-zero results in the same fitted parameters within the errors.

where λ is in Å. Given a measured Hα/Hβ flux ratio, the optical depth at any wavelength can be obtained from

$$\tau_\lambda = 3.22 \ln \left[\frac{2.86}{f(\text{H}\alpha)/f(\text{H}\beta)} \right] \frac{\tau_\lambda}{\tau_V}, \tag{8}$$

where τ_λ/τ_V is given in equation (7), $A_\lambda = 1.086\tau_\lambda$ is the attenuation in magnitudes and a Case B recombination ratio of 2.86 is assumed.

4.3 Dense versus diffuse dust

Extinction in the mid-IR continuum is dominated by the stretching and bending modes of amorphous silicate grains with two strong features at 9.7 and 18 μm. Importantly for this section, it is evident from the many theoretical models that *any* significant silicate absorption, as found in the ULIRGs and many of the Balmer-strong galaxies, implies optical extinction at levels of $\tau_V \sim 50$–100 (e.g. Sirocky et al. 2008; Rowan-Robinson & Efstathiou 2009). It is therefore impossible for ionizing UV continuum and associated line radiation to pass through these clouds directly.

In Fig. 7, we plot the Balmer decrement [Hα/($B \times$Hβ), where B is the unattenuated ratio] against the 9.7-μm silicate absorption strength for all four samples. For H II regions, we set $B = 2.86$ for Case B recombination at 10 000 K and electron density of 10^2–10^4/cm^{-3} (Osterbrock & Ferland 2006). For AGNs, we set $B = 3.1$ (Kewley et al. 2006). Surprisingly, we see a correlation between these two measures of dust content for most galaxies in our samples. However, it is clear that they do not trace the *same* dust, because the τ_V measured from the Balmer emission lines (upper axis) is an order of magnitude lower than that indicated by the mid-IR silicate absorption strengths (right-hand axis, from zero-age starburst models of Rowan-Robinson & Efstathiou 2009). The dotted line is the
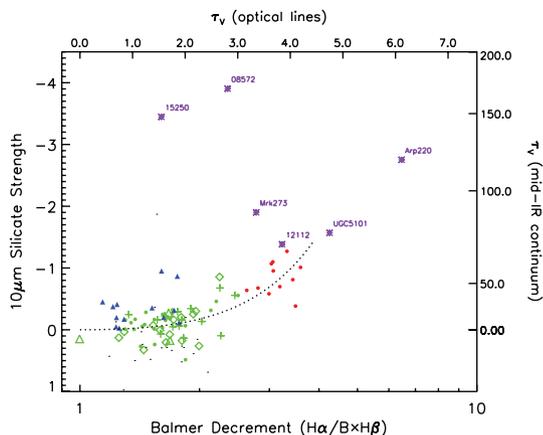

Figure 7. The optical Balmer decrement versus silicate 9.7-μm absorption strength. The Balmer decrement is defined with an intrinsic ratio of $B = 2.86$ (3.1) for galaxies classed as star-forming/composite (AGNs) from their optical emission lines. Thus, a Balmer decrement of 1 indicates no optical dust attenuation. The top axis indicates the corresponding optical τ_V, assuming the best-fitting $\mu_{0.4}$ dust curve derived in Section 4.2. The right-hand axis indicates the corresponding mid-IR τ_V from the zero-age starburst models of Rowan-Robinson & Efstathiou (2009). Overplotted as a dotted line is the best-fitting relation to the SSGSS-star-forming, composite and Balmer-strong galaxies as described in the text. Only those galaxies with Hα and Hβ detected at $>3\sigma$ and mean per-pixel-S/N > 2 between 5.4 and 5.9 μm are plotted. Symbols are: SSGSS star-forming galaxies (green dots, 25/35), SSGSS AGNs (green open triangles, 3/4), SSGSS composite galaxies (green open diamonds, 14/21), Balmer-strong galaxies (red dots, 11/11), ULIRGs (purple stars, 6/6) and Seyferts (blue triangles, 13/20).

best-fitting squared relation to the SSGSS-star-forming, composite and Balmer-strong galaxies:

$$\text{Sil}_{9.7\,\mu\text{m}} = -0.17 \left[\frac{f(\text{H}\alpha)}{Bf(\text{H}\beta)} - 1 \right]^2. \tag{9}$$

In the case of star-forming galaxies without a strong AGN, the mid-IR continuum predominantly arises from dust grains situated within the H II regions, re-radiating the light from young and hot stars. It is this dust continuum that is absorbed by the silicate grains along the line of sight between the light source and the observer. Balmer emission lines also come from ionized gas within H II regions. Thus, the observed correlation between the silicate absorption strength and Balmer decrement implies either: (i) a correlation between the amount of dust in dense stellar birth clouds, which causes silicate absorption, and the amount of dust in more diffuse stellar birth clouds, which causes absorption of the optical emission lines; or (ii) a self-similar structure for H II regions in which the Balmer lines that reach the observer have passed through a fixed fraction of the dense dust clouds.

There are two notable exceptions, where the optical Balmer decrement fails to predict the presence of an extremely significant attenuation in the mid-IR: the ULIRGs 15250 and 08572. Nardini et al. (2009) found that both of these ULIRGs have significant contributions from AGNs to their bolometric luminosity (53 and 87 per cent, respectively), using a spectral decomposition between 5 and 8 μm. Models have shown that extremely strong silicate absorption, as observed in these two ULIRGs, requires a steep temperature gradient within the obscuring cloud, which can only be obtained where the light source responsible for heating the dust that causes the mid-IR continuum is deeply buried in a smooth thick shell of dust that is both geometrically and optically thick (Levenson et al. 2007). This is again consistent with the source being an AGN, although a nuclear starburst may suffice. A clumpy distribution of dust leads to much shallower absorption or emission (Nenkova, Ivezić & Elitzur 2002). Our emission-line analysis is also consistent with these galaxies harbouring a buried AGN. They have an increased [Ne]/Hα ratio and lie in the composite region of the BPT diagram. While the position of these galaxies on the BPT diagram is not in itself a conclusive proof that these two ULIRGs harbour an AGN, if their position is caused by the AGN, then it indicates that ionizing radiation from the AGN escapes to ionize the NLR, despite the dense dust cloud that presumably surrounds the central continuum source. Two dusty Seyfert galaxies and one ULIRG with a Seyfert nucleus (Mrk273) also lie above the relation defined by the SSGSS and Balmer-strong galaxies, further supporting the idea that dust along the line of sight to a deeply buried AGN can lead to stronger silicate absorption, relative to nebular line absorption, than normal H II regions.

We are not aware of any models, which simultaneously predict the strength of silicate absorption and attenuation of the optical emission lines. Qualitatively, Fig. 7 suggests that a two-component model is required to describe the dust distribution in galaxies/AGNs. The lower branch is consistent with silicate absorption arising in the clumpy distribution of stellar birth clouds, with the densest clouds causing some silicate absorption, and the Balmer emission lines originating from the same star formation regions, but farther out in the clouds. The upward scatter of some sources from this branch is consistent with the dust being concentrated in a dense shell-like distribution obscuring a single nuclear source, most likely an AGN in the cases studied here, but also conceivably a strong nuclear starburst.
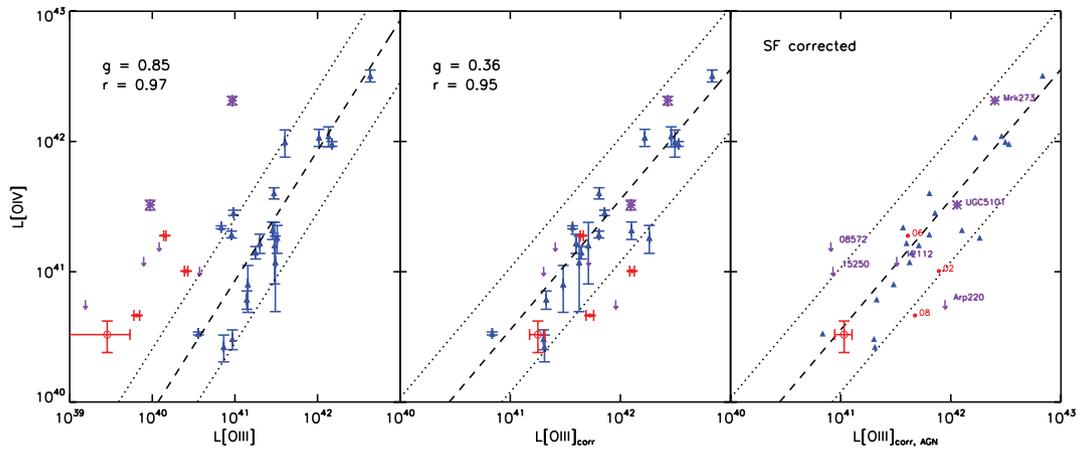
Figure 8. [O III] λ5008 Å versus [O IV] λ26 μm luminosities (erg s⁻¹) for the Seyfert sample (filled blue triangles, 20/20), ULIRGs (purple stars, 2/6) and the Balmer-strong galaxies (red circles, 3/11) with [O IV], [O III], Hα and Hβ detected at >3σ. The stack of the remaining Balmer-strong galaxies with non-detections in [O IV] is shown as a red open circle. Left-hand panel: L[O III] is not corrected for dust attenuation or for contamination due to star formation. Note the different *x*-axis range in this panel. Middle panel: L[O III] is corrected for dust attenuation, but not for contamination due to star formation. Right-hand panel: L[O III] of the ULIRGs and Balmer-strong galaxies has been corrected for contamination from star formation using the method described in Wild et al. (2010). Dust attenuation is calculated using the best-fitting dust curve derived in Section 4.2. Overplotted as a dashed line is the best-fitting linear relation to the Seyfert sample only; the dotted lines indicate a factor of 3 above and below this relation. For clarity, error bars are omitted in the right-hand panel.

4.4 Galaxies with an AGN

As explained in Section 2.1, a dust curve and accurate Balmer decrement that adequately corrects H II region emission lines for dust attenuation will not necessarily do the same for lines from the NLR of AGNs. Particularly in composite objects, a higher fraction of Balmer lines will arise from within the H II regions of the galaxy compared to lines, such as [O III], which are stronger in NLRs. Therefore, a form of differential extinction might arise between the Balmer and higher ionization lines, and a corresponding bias in the correction of AGN NLR lines for dust using the measured Balmer decrement. Additionally, the form of the dust curve may not be the same for light originating from H II regions and from an AGN NLR, due to the different relative geometry between the light source and the dust cloud, and the different balance between dense and diffuse dust attenuating the lines. The mid-IR [O IV] line at 25.89 μm has been shown to be an accurate indicator of AGN power (Meléndez et al. 2008) and the [O III]/[O IV] ratio a possible measure of AGN attenuation (Haas et al. 2005). In this section, we test the accuracy of dust-corrected L[O III] as a measure of AGN luminosity in our sources by comparing with the mid-IR [O IV] line.

In Fig. 8, we plot dust-uncorrected and dust-corrected L[O III] versus L([O IV] λ26 μm) for the Seyferts, the three Balmer-strong galaxies and the two ULIRGs with measured [O IV] lines. Note that the correlation coefficient is similar for the Seyferts whether the dust correction is performed or not. These Seyferts have very small Balmer decrements, so the dust correction has only a small effect. Because some of these objects are classified as composite AGN–star formation by their optical line ratios and [O III] is also produced by star formation, in the right-hand panel, we apply a correction for this following the method of Wild, Heckman & Charlot (2010), based on the expected [O III]/Hα ratio for metal-rich star-forming galaxies.[14] [O IV] is also produced in H II regions, although the contamination is expected to be much smaller than for [O III] due to

the higher ionization level. Clearly, there is a tight correlation between dust-corrected L[O III] and L[O IV] for the Seyfert sample (see also LaMassa et al. 2010). All of the dusty Balmer-strong galaxies and ULIRGs with measured [O IV] fall within a factor of 3 of the relation defined by the Seyferts. Only the upper limit for Arp 220 is marginally inconsistent with the relation defined by the Seyfert galaxies. Taking the remainder of the Balmer-strong galaxies and stacking the SH spectra in luminosity units shows a clear [O IV] line, which we fit together with the neighbouring Fe II line using a double Gaussian. The corresponding stacked L[O IV]–L[O III] luminosity also lies exactly on the Seyfert relation, once contamination of L[O III] from star formation has been accounted for. Errors are estimated from the standard deviation of the luminosity on removing one spectrum at a time from the stack. This strong correlation between [O IV] and [O III] dust corrected using the observed Balmer decrement and dust curve appropriate for H II regions, for even dusty composite galaxies, shows that there is no evidence for significant differential extinction between lines emitted from the NLR and H II regions of a galaxy. Although slightly surprising, this may imply that the majority of dust attenuation suffered by NLR emission lines comes from the diffuse dust and H II regions in the intervening galaxy, through which they must pass on their way to the observer.

Unfortunately, neither of the two ULIRGs with extreme silicate absorption (08572 and 15250) have measured L[O IV], so we cannot test directly whether optical and mid-IR NLR lines agree even in the presence of extreme, dense obscuration of the central light source. Such a study may be possible with the large samples of ULIRGs now available in archives.

5 DISCUSSION

The potential of dust attenuation and complicated dust geometries to render useless optical observations of extreme galaxies is sometimes used to justify rest-frame IR observations. In the previous sections, we have used the correlation between the unattenuated mid-IR and attenuated optical nebular emission lines to argue that a single dust curve can accurately correct optical emission lines for

---

[14] We note that such a correction would not be appropriate for the ULIRGs, if shocks were a significant contributor to the total Hα luminosity.
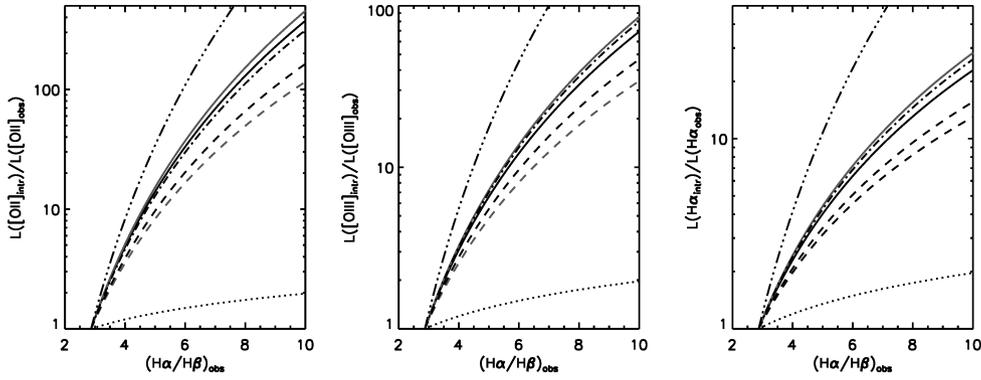
Figure 9. Intrinsic to observed flux ratios as a function of the observed Hα/Hβ line ratio for different dust curves, at wavelengths corresponding to [O II] λλ3727, 3730 (left-hand panel), [O III] λ5008 Å (middle panel) and Hα (right-hand panel). The lines are (as given in Fig. 6): the SMC extinction curve with an $R_V = 3.1$ (dotted, Pei 1992); an MW extinction curve with $R_V = 3.1$ (dashed black, O'Donnell 1994); a different MW extinction curve with $R_V = 3.2$ (dashed grey, Seaton 1979; Nandy et al. 1975);; the $\mu_{0.3}$ and $\mu_{0.4}$ attenuation curves for emission lines (solid black and grey, Wild et al. 2007); the Calzetti attenuation curve for starburst continua with $R_V = 4.05$ (dot–dashed, Calzetti et al. 2000); and the $\lambda^{-0.7}$ attenuation curve for starburst continua from CF00 (dash–triple-dotted). *Note the changing scale on the y-axis.*

dust attenuation in a large range of different galaxies. The correction is accurate to within a factor of 2 in most cases, and to at least a factor of 4 for even the most heavily obscured ULIRGs.

Here, we discuss the implications of our work for deriving SFRs and BHARs from the optical emission lines Hα, [O II] and [O III]. We present useful relations for dust corrections at the wavelengths of each of these lines.

5.1 Star formation rates

The left-hand and right-hand panels of Fig. 9 show the fractional attenuation (in flux units) as a function of the observed Balmer decrement at Hα and [O II], for each of the different dust curves discussed in Section 4. Using the best-fitting $\mu_{0.4}$ dust curve, the recommended correction at Hα is

$$L[\mathrm{H}\alpha]_{\mathrm{corr}} = L[\mathrm{H}\alpha]_{\mathrm{obs}} \left[\frac{(\mathrm{H}\alpha/\mathrm{H}\beta)_{\mathrm{obs}}}{B} \right]^{2.67^{+0.40}_{-0.32}} \tag{10}$$

and at [O II][15]

$$L[\mathrm{O\,II}]_{\mathrm{corr}} = L[\mathrm{O\,II}]_{\mathrm{obs}} \left[\frac{(\mathrm{H}\alpha/\mathrm{H}\beta)_{\mathrm{obs}}}{B} \right]^{4.89^{+0.36}_{-0.29}}, \tag{11}$$

where B is the unattenuated ratio as discussed above and errors are propagated from the errors on the best-fitting μ. While for H II galaxies and strong Seyferts the choice of B is clear, for composite galaxies, the unknown B may cause small systematic uncertainties. However, as H II regions have relatively stronger Hα emission, a value of $B = 2.86$ is probably close to reality.

To derive an SFR from optical nebular emission lines, two steps are required. This paper has focused on the first step: to correct the line for dust attenuation. The second step is to convert the dust-corrected line luminosity into an SFR. While our results show that dust-corrected Hα luminosity traces [Ne] luminosity, this is not enough to confirm the reliability of Hα as an indicator of the SFR in extremely dusty objects. This is because dense dust clouds can have high optical depths even in the mid-IR, as indicated by the strong silicate absorption in some galaxies, and thus even the neon lines

[15] Note that this is an extrapolation of the dust curve beyond the wavelength region directly tested in this paper.

may be attenuated in some objects. In addition, the most extreme compact, dusty galaxies may even have a non-negligible fraction of their ionizing photons absorbed by dust and not gas (and thus not traced by Hα). Encouragingly, Ho & Keto (2007) have already shown how [Ne] luminosity correlates strongly with both the total IR luminosity and Brackett α luminosity in star-forming galaxies. Their galaxy sample includes a handful of ULIRGs, showing that these relations hold even at extreme luminosities. This result provides circumstantial evidence that the neon luminosity is tracing star formation even in the dustiest of galaxies. In contrast, Farrah et al. (2007) found [Ne] luminosity in ULIRGs to be deficient by 0.4 dex from the Ho & Keto relation, which they ascribed to extinction of the [Ne] lines. In a companion paper, we plan to address this issue directly by comparing the SFRs derived from the full SEDs with that derived from the emission lines.

5.2 Black hole accretion rates

As with the SFR, the derivation of BHARs from nebular emission-line luminosities requires two steps: correction for dust emission discussed in this paper and then conversion into BHAR via a bolometric correction.

For the best-fitting $\mu_{0.4}$ dust curve, the relevant correction for dust attenuation at [O III] is

$$L[\mathrm{O\,III}]_{\mathrm{corr}} = L[\mathrm{O\,III}] \left[\frac{(\mathrm{H}\alpha/\mathrm{H}\beta)_{\mathrm{obs}}}{B} \right]^{3.55^{+0.40}_{-0.32}}, \tag{12}$$

where B is the unattenuated ratio as discussed above. The correction caused by the different dust curves is presented in the middle panel of Fig. 9.

The exponent for the $\mu_{0.4}$ dust curve is larger than that used in some AGN literature and can lead to significant differences in estimated bolometric AGN luminosity and accretion rates as a fraction of L_{Edd} (see also the discussion in Netzer 2009). Using a smaller exponent than appropriate will cause an underestimate in $L[\mathrm{O\,III}]_{\mathrm{corr}}$, which will vary with dust content. For example, for the relatively dust-free sample of Seyfert galaxies studied in this work, the difference between the $\mu_{0.4}$ dust curve exponent of 3.55 and 2.94 (from an MW extinction law) used in, for example, Bassani et al. (1999) and Lamastra et al. (2009), leads to differences ranging from 5 to 30 per cent. The potential increase in the under- (or over-)estimation of

the line luminosity with increasing dust content because of an inappropriate dust curve has important implications for understanding whether the bolometric correction for L[O III] changes systematically with L[O III], due to the correlations between the SFR of the host galaxy and the luminosity of the central AGN (e.g. Kauffmann et al. 2003; Schweitzer et al. 2006; Netzer 2009; Zheng et al. 2009) and the SFR and dust content of the host (da Cunha et al. 2010). Our results do not explicitly constrain which dust curve is most appropriate for Seyferts; however, we would like to emphasize the importance of including the errors caused by the dust-attenuation correction when studying emission-line trends.

5.3 AGN detection

Even in the two ULIRGs in our sample, where there is evidence for a heavily buried central nucleus, we would like to emphasize that the optical emission-line ratios still indicate the possible presence of an AGN, albeit not conclusively. This shows that even where the AGN is deeply buried, some radiation may still escape to ionize the NLR clouds. This has important implications for using optical emission-line ratios to identify AGNs in objects, such as ULIRGs, and will become increasingly important at high z. Unfortunately, neither of the two ULIRGs with strong silicate absorption in our sample have measured [O IV] and therefore we cannot directly verify that their position on the BPT diagram, and therefore their correction of [O III] for contamination from star formation, is correct. The specific study of a larger sample of ULIRGs to compare the bolometric AGN luminosities derived from mid-IR lines, mid-IR continuum and dust- and star-formation corrected high-quality optical emission lines would now be possible with samples in the SDSS and *Spitzer* archives.

6 CONCLUSIONS

The purpose of this paper was to verify, or otherwise, the accuracy of fundamental quantities derived from optical emission lines, particularly in the case of significant dust attenuation of the lines. In particular, optical emission lines provide powerful measures of the SFR and BHAR. We compared two 'dusty' galaxy samples, including six ULIRGs, to a sample of 'ordinary' galaxies from the SSGSS all with high-quality SDSS optical spectra and mid-IR spectra from the *Spitzer Space Telescope* IRS spectrograph. The results are extremely encouraging for using rest-frame optical spectra to study dusty galaxies with an $A_V < 4.5$. Our results are promising even for galaxies as dusty as ULIRGs, although a much larger sample should be studied covering the full range of this diverse population, in order to verify our conclusions. Our results have important implications for future high-redshift spectroscopic surveys, where galaxies have higher SFRs and dust contents may be correspondingly higher.

We have compared several different dust curves used in the literature to correct optical emission lines for dust attenuation. Our results favour a dust curve, which lies close to the MW extinction curve, indicating that a significant fraction of the dust, which attenuates nebular emission lines, has a screen-like geometry. This is in agreement with the model for emission-line attenuation presented by Wild et al. (2007) and da Cunha et al. (2008) and based upon the two-component CF00 dust model. In this model, the screen-like extinction arises from the dense stellar birth clouds, which surround the hottest stars responsible for ionizing the gas. We find a best-fitting dust curve with on average 40 per cent of the optical depth at 5500 Å arising from diffuse ISM dust. The $\mu_{0.4}$ dust curve is

not significantly different from the Calzetti dust curve in the optical wavelength regime; however, we focus our results and analysis on the former, which was intended for emission lines and allows greater flexibility, rather than the latter, which was derived from galaxy continua.

Particular conclusions with regard to measuring star formation from optical emission lines in the presence of dust are as follows:

(i) The MW, Calzetti, $\mu_{0.3}$ and best-fitting $\mu_{0.4}$ dust curves all allow accurate correction of Hα (to better than a factor of 2), and therefore accurate calculation of SFRs, for galaxies with observed Hα/Hβ ratios of as much as 10 ($\tau_V < 4.5$).

(ii) For only 2/6 ULIRGs with $\tau_V < 6$ does the optical Hα differ from the mid-IR [Ne] lines by more than a factor of 2, but then only by a factor of 4. In these two cases (08572 and 15250), we have argued that the observed excess of [Ne] is in fact caused by a buried AGN, rather than uncertainties in the dust correction (in agreement with the results of Nardini et al. 2009).

(iii) The majority of galaxies in our samples favour a dust curve close to the MW screen-like dust extinction curve. This suggests that much of the extra dust in the unusually dusty objects is located in dense clouds, rather than in the diffuse ISM.

(iv) There is tentative evidence for a range in the shape of the dust curves in ordinary star-forming galaxies. For the CF00 dust model, this range translates into a variation in the fraction of the optical depth arising in the diffuse ISM of between around 30 and 90 per cent, with the remaining fraction arising in dense birth clouds. However, the variation in the intrinsic [Ne]/Hα ratio with metallicity, the issue of relative aperture correction between the IRS and SDSS data and the large statistical errors on the Hβ emission line, prevent us from quantifying this scatter more precisely.

Particular conclusions with regard to identifying AGNs and measuring their accretion rates from optical emission lines in the presence of dust are as follows:

(i) The best-fitting $\mu_{0.4}$ dust curve and measured Balmer decrement allows accurate correction of [O III] for dust attenuation to within a factor of 3. This is slightly surprising and suggests that the effects of variations in the relative geometry of the source and dust, and differential extinction between the Balmer and higher ionization lines, are minimal.

(ii) The method to separate the contributions to optical emission lines from both star formation and AGN presented in Wild et al. (2010) tightens the relation between L[O IV] and L[O III] for composite objects. This supports the use of the position of galaxies on the optical BPT line ratio diagram to measure the amount of L[O III] originating from the AGN and therefore the estimates of BHARs from L[O III] corrected for dust attenuation and star formation contamination.

(iii) All ULIRGs in our sample are classified as AGNs or composite objects from their optical emission-line ratios. While the composite line ratios may be caused by shocks, we have argued that other observational results favour the presence of a buried AGN contributing significantly to the mid-IR continuum. It is therefore possible that sufficient ionizing flux escapes from the central source to ionize the NLR, even in the case of heavily buried nuclei, such as in ULIRGS 08572 and 15250. Unfortunately, these two ULIRGs do not have measured L[O IV], preventing us from verifying our corrections to L[O III] for dust attenuation and star formation contamination in such extreme cases. In the case of ULIRGs, whose properties vary widely, clearly a much larger sample should be studied before firm conclusions can be drawn.

ACKNOWLEDGMENTS

REFERENCES

Adelman-McCarthy J. K. et al., 2008, ApJS, 175, 297
Armus L. et al., 2007, ApJ, 656, 148
Baldwin J. A., Phillips M. M., Terlevich R., 1981, PASP, 93, 5
Bassani L., Dadina M., Maiolino R., Salvati M., Risaliti G., della Ceca R., Matt G., Zamorani G., 1999, ApJS, 121, 473
Böker T. et al., 1999, ApJS, 124, 95
Borgne D. L., Elbaz D., Ocvirk P., Pichon C., 2009, A&A, 504, 727
Brinchmann J., Charlot S., White S. D. M., Tremonti C., Kauffmann G., Heckman T., Brinkmann J., 2004, MNRAS, 351, 1151
Bruzual G., Charlot S., 2003, MNRAS, 344, 1000
Calzetti D., 2001, PASP, 113, 1449
Calzetti D., Kinney A. L., Storchi-Bergmann T., 1994, ApJ, 429, 582
Calzetti D., Kinney A. L., Storchi-Bergmann T., 1996, ApJ, 458, 132
Calzetti D., Armus L., Bohlin R. C., Kinney A. L., Koornneef J., Storchi-Bergmann T., 2000, ApJ, 533, 682
Cardelli J. A., Clayton G. C., Mathis J. S., 1989, ApJ, 345, 245
Charlot S., Fall S. M., 2000, ApJ, 539, 718 (CF00)
da Cunha E., Charlot S., Elbaz D., 2008, MNRAS, 388, 1595
da Cunha E., Eminian C., Charlot S., Blaizot J., 2010, MNRAS, 403, 1894
Díaz-Santos T., Alonso-Herrero A., Colina L., Packham C., Levenson N. A., Pereira-Santaella M., Roche P. F., Telesco C. M., 2010, ApJ, 711, 328
Eliche-Moral M. C., Prieto M., Gallego J., Zamorano J., 2010, arXiv:1003.0686
Farrah D. et al., 2007, ApJ, 667, 149
Fernandes R. C., Stasińska G., Schlickmann M. S., Mateus A., Asari N. V., Schoenell W., Sodré L., 2010, MNRAS, 403, 1036
Groves B. A., Allen M. G., 2010, New Astron., 15, 614
Groves B. A., Dopita M. A., Sutherland R. S., 2004, ApJS, 153, 75
Groves B. A., Heckman T. M., Kauffmann G., 2006, MNRAS, 371, 1559

Haas M., Siebenmorgen R., Schulz B., Krügel E., Chini R., 2005, A&A, 442, L39
Heckman T. M., Kauffmann G., Brinchmann J., Charlot S., Tremonti C., White S. D. M., 2004, ApJ, 613, 109
Higdon S. J. U. et al., 2004, PASP, 116, 975
Higdon S. J. U., Armus L., Higdon J. L., Soifer B. T., Spoon H. W. W., 2006, ApJ, 648, 323
Ho L. C., Keto E., 2007, ApJ, 658, 314
Hopkins P. F., Hernquist L., Cox T. J., Matteo T. D., Robertson B., Springel V., 2006, ApJS, 163, 1
Houck J. R. et al., 2004, ApJS, 154, 18
Ilbert O. et al., 2010, ApJ, 709, 644
Johnson B. D., Schiminovich D., O'Dowd M., Meder K., Treyer M., 2009, in Sheth K., Noriega-Crespo A., Ingalls J., Paladini R., eds, The Evolving ISM in the Milky Way and Nearby Galaxies, p. 31 (http://ssc.spitzer.caltech.edu/mtgs/ismevol/)
Kauffmann G. et al., 2003, MNRAS, 346, 1055
Kauffmann G. et al., 2003, MNRAS, 341, 33
Kennicutt R. C. et al., 2009, ApJ, 703, 1672
Kewley L. J., Dopita M. A., Sutherland R. S., Heisler C. A., Trevena J., 2001, ApJ, 556, 121
Kewley L. J., Groves B., Kauffmann G., Heckman T., 2006, MNRAS, 372, 961
LaMassa S. M., Heckman T. M., Ptak A., Hornschemeier A., Martins L., Sonnentrucker P., Tremonti C., 2009, ApJ, 705, 568
LaMassa S. M., Heckman T. M., Ptak A., Martins L., Wild V., Sonnentrucker P., Tremonti C., 2010, ApJ, 720, 786
Lamastra A., Bianchi S., Matt G., Perola G. C., Barcons X., Carrera F. J., 2009, A&A, 504, 73
Levenson N. A., Sirocky M. M., Hao L., Spoon H. W. W., Marshall J. A., Elitzur M., Houck J. R., 2007, ApJ, 654, L45
Levesque E. M., Kewley L. J., Larson K. L., 2010, AJ, 139, 712
Markwardt C. B., 2009, in Bohlender D. A., Durand D., Dower P., eds, ASP Conf. Ser. Vol. 411, Astronomical Data Analysis Software and Systems XVIII. Astron. Soc. Pac., San Francisco, p. 251
Meléndez M. et al., 2008, ApJ, 682, 94
Muzzin A., Marchesini D., van Dokkum P. G., Labbé I., Kriek M., Franx M., 2009, ApJ, 701, 1839
Naab T., Khochfar S., Burkert A., 2006, ApJ, 636, L81
Nandy K., Thompson G. I., Jamar C., Monfils A., Wilson R., 1975, A&A, 44, 195
Nardini E., Risaliti G., Salvati M., Sani E., Watabe Y., Marconi A., Maiolino R., 2009, MNRAS, 399, 1373
Narron R., Ogle P., Laher R. R., 2007, in Shaw R. A., Hill F., Bell D. J., eds, ASP Conf. Ser. Vol. 376, Astronomical Data Analysis Software and Systems XVI. Astron. Soc. Pac., San Francsico, p. 437
Nenkova M., Ivezić Ž., Elitzur M., 2002, ApJ, 570, L9
Netzer H., 2009, MNRAS, 399, 1907
O'Donnell J. E., 1994, ApJ, 422, 158
O'Dowd M. J. et al., 2009, ApJ, 705, 885
Ogle P., Boulanger F., Guillard P., Evans D. A., Antonucci R., Appleton P. N., Nesvadba N., Leipski C., 2010, ApJ, in press (arXiv:1009.4533)
Osterbrock D. E., Ferland G. J., 2006, Astrophysics of Gaseous Nebulae and Active Galactic Nuclei. University Science Books, Sausalito, CA
Pei Y. C., 1992, ApJ, 395, 130
Poggianti B. M., Wu H., 2000, ApJ, 529, 157
Rocha M., Jonsson P., Primack J. R., Cox T. J., 2008, MNRAS, 383, 1281
Rowan-Robinson M., Efstathiou A., 2009, MNRAS, 399, 615
Salim S. et al., 2005, ApJ, 619, L39
Sánchez-Blázquez P. et al., 2006, MNRAS, 371, 703
Sanders D. B., Soifer B. T., Elias J. H., Madore B. F., Matthews K., Neugebauer G., Scoville N. Z., 1988, ApJ 325, 74
Schweitzer M. et al., 2006, ApJ, 649, 79
Seaton M. J., 1979, MNRAS, 187, 73P
Silva L., Granato G. L., Bressan A., Danese L., 1998, ApJ, 509, 103
Sirocky M. M., Levenson N. A., Elitzur M., Spoon H. W. W., Armus L., 2008, ApJ, 678, 729
Smith J. D. T. et al., 2007, ApJ, 656, 770

Soifer B. T., Sanders D. B., Madore B. F., Neugebauer G., Danielson G. E., Elias J. H., Lonsdale C. J., Rice W. L., 1987, ApJ, 320, 238

Spoon H. W. W., Marshall J. A., Houck J. R., Elitzur M., Hao L., Armus L., Brandl B. R., Charmandaris V., 2007, ApJ, 654, L49

Stasińska G., Asari N. V., Fernandes R. C., Gomes J. M., Schlickmann M., Mateus A., Schoenell W., Sodré L., 2008, MNRAS, 391, L29

Veilleux S., Kim D.-C., Sanders D. B., 2002, ApJS, 143, 315

Wild V., Kauffmann G., Heckman T., Charlot S., Lemson G., Brinchmann J., Reichard T., Pasquali A., 2007, MNRAS, 381, 543

Wild V., Walcher C. J., Johansson P. H., Tresse L., Charlot S., Pollo A., Fèvre O. L., de Ravel L., 2009, MNRAS, 395, 144

Wild V., Heckman T., Charlot S., 2010, MNRAS, 405, 933

Wild V. et al., 2010, in Peterson B. M., Somerville R. S., Storchi-Bergmann T., eds, Proc. IAU Symp. 267, Co-evolution of Central Black Holes and Galaxies. Cambridge Univ. Press, Cambridge, p. 96

Yu Q., Tremaine S., 2002, MNRAS, 335, 965

Zheng X. Z. et al., 2009, ApJ, 707, 1566

APPENDIX A: SAMPLE INFORMATION

APPENDIX B: BALMER-STRONG GALAXIES

While three of the samples studied in this paper have been presented elsewhere, the Balmer-strong sample has not. Here we summarize its selection criteria and the mid-IR observations.

B1 Selection

The galaxies were selected to have:

(i) Observed Hα/Hβ flux ratios greater than 8

(ii) Strong Balmer absorption lines compared to their 4000 Å break strength (PC2 > 0.05 × PC1 + 0.4, Wild et al. 2007).

Although they were not selected on a single Balmer absorption line EW, which have considerably larger errors than the spectral indices used here, most have Hδ_A > 5 Å and $D_n(4000)$ < 1.4.

(iii) Accurately measured emission lines: an S/N > 3σ for all four BPT lines, together with a Hβ flux > 40×10^{-17} erg s^{-1} cm^{-2}.

(iv) A contribution to their emission lines by an AGN, that is, they lie above the empirically derived demarcation line of Kauffmann et al. (2003) on the BPT diagram.

(v) $z < 0.07$, so that the SDSS spectrum, taken through a 3-arcsec fibre, samples only light coming from the central few kpc of the galaxy.

B2 Mid-IR observations

IRS observations in both high and low resolution were carried out using staring mode during program 40330 (PI Timothy Heckman).

We used SPICE to extract the 1D spectra from the low-resolution basic calibrated data pipeline products, using the point-source and optimal extraction options. The two 1D spectra (i.e. one for each nod) were combined using a weighted mean. For the high-resolution spectra, we first identified and interpolated over additional rogue pixels using a custom IDL routine and the rogue pixel masks suitable for our campaign numbers (41–46). This procedure was repeated for the dedicated off-source background observations. All three science exposures were combined using a simple arithmetic mean, resulting in two 2D spectra. These were sky-subtracted and the 1D spectra were extracted using SPICE with the point-source and optimal extraction options. For each nod, the edges of each order were inspected and trimmed and the orders combined using a weighted mean, where wavelengths were covered by more than one order. The 1D spectra of each nod were subsequently combined using a weighted mean.

Table A1. The Balmer-strong sample. Columns are: name (1), RA (2), Dec. (3), SDSS specobjid (4), SDSS-MPA rowindex (5) and redshift from SDSS (6).

Name	RA (°)	Dec. (°)	specobjid	rowindex	z
PSB01	181.225	52.395	248485859366535168	284940	0.0632
PSB02	169.600	56.036	256085720727289856	296570	0.0680
PSB03	173.251	60.275	268189274979958784	315471	0.0644
PSB04	167.291	45.857	404988882665340928	491844	0.0636
PSB05	136.004	1.458	132797726868897792	105860	0.0535
PSB06	120.199	37.729	213582458531086336	232315	0.0416
PSB07	339.726	13.194	208235580251701248	223368	0.0628
PSB08	128.311	32.583	262560681922920448	306604	0.0558
PSB09	239.431	27.465	391758540508758016	472114	0.0316
PSB10	139.864	33.791	448335754997792768	536057	0.0193
PSB11	158.162	12.178	450306505485320192	539391	0.0329

Table A2. The ULIRG sample, where SDSS spectra exist. Columns are: name as given in Armus et al. (2007) (1), RA (2), Dec. (3), SDSS specobjid (4), SDSS-MPA rowindex (5) and redshift from SDSS (6).

Name	RA (°)	Dec. (°)	specobjid	rowindex	z
IRAS 08572+3915	135.106	39.065	337714854909444096	394321	0.0579
IRAS 12112+0305	183.441	2.811	146028589375029248	126942	0.0730
IRAS 15250+3609	231.748	35.977	394574695615168512	476759	0.0553
Arp 220	233.738	23.504	609061542893191168	755340	0.0181
Mrk 273	206.176	55.887	372055066565148672	439991	0.0373
UGC 5101	143.965	61.353	137019791402598400	111495	0.0393

Table A3. The Seyfert sample. Columns are: name as given in LaMassa et al. (2010) (1), RA (2), Dec. (3), SDSS specobjid (4), SDSS-MPA rowindex (5) and redshift from SDSS (6).

Name	RA (°)	Dec. (°)	specobjid	rowindex	z
2MASX J08244333+2959238	126.180	29.990	339966523504328704	397741	0.0250
CGCG 064−017	149.812	12.988	491120230488080384	603606	0.0340
Mrk 0609	51.356	−6.144	129701503752470528	101843	0.0340
NCG 0291	13.375	−8.768	185153160128495616	190581	0.0190
NGC 5695	219.342	36.568	389226545811554304	467780	0.0140
2MASX J15522564+2753435	238.107	27.895	391758541012074496	472216	0.0740
2MASX J12384342+0927362	189.681	9.460	347285137836212224	409636	0.0830
2MASX J08035923+2345201	120.997	23.756	356292212926971904	415287	0.0290
2MASX J16164729+3716209	244.197	37.273	297464197648744448	366718	0.1520
2MASX J11570483+5249036	179.270	52.818	248485858699640832	284823	0.0360
2MASX J12183945+4706275	184.664	47.108	408648327781941248	498207	0.0940
SBS 1133+572	173.954	56.952	369240319515951104	435171	0.0510
SBS 1609+490	242.716	48.911	175301007746531328	174339	0.0450
IC 0486	120.087	26.614	261716087635181568	305068	0.0270
CGCG 242−028	170.755	47.052	405833433537839104	493622	0.0250
Mrk 1457	176.840	52.450	247922896524017664	283914	0.0490
2MASX J13463217+6423247	206.634	64.390	170234565783191552	166011	0.0240
CGCG 218−007	200.952	43.301	387537584101785600	464960	0.0270
2MASX J10181928+3722419	154.580	37.378	401892408733728768	486221	0.0490
2MASX J11110693+0228477	167.779	2.480	143495710086529024	122473	0.0350

This paper has been typeset from a TEX/LATEX file prepared by the author.